ADVANCING EARTH AND SPACE SCIENCES

JGR Solid Earth

RESEARCH ARTICLE

10.1029/2025JB033035

Geodetic Constraints on Fault Kinematics and Dynamics of 2021 Maduo Earthquake: Implications for Fault Friction

Yuan Gao[1,2,3], Qi Ou[4], Jin Fang[2], Manon Carpenter[2], Tim J. Wright[2], Kali Allison[5], Wei Qu[3], Qin Zhang[3], Milan Lazecký[2], Yasser Maghsoudi[6], and Zhong Lu[1,7]

[1]School of Environment and Spatial Informatics, China University of Mining and Technology, Xuzhou, China, [2]COMET, School of Earth, Environment and Sustainability, University of Leeds, Leeds, UK, [3]College of Geology Engineering and Geomatics, Chang'an University, Xi'an, China, [4]COMET, School of Geosciences, University of Edinburgh, Edinburgh, UK, [5]Earth and Planetary Sciences department, University of California Davis, Davis, CA, USA, [6]COMET, Department of Earth and Environmental Sciences, University of Exeter, Cornwall, UK, [7]Roy M. Huffington Department of Earth Sciences, Southern Methodist University, Dallas, TX, USA

Key Points:

- Significant postseismic afterslip of the Maduo earthquake occurs on shallow part of fault that also had large coseismic slip
- Numerical models indicate velocity-strengthening friction in shallow region can slip seismically and aseismically
- We do not observe clear interseismic strain localization or creep on fault, which is either absent or too low to be detected

Supporting Information:

Supporting Information may be found in the online version of this article.

Correspondence to:

Y. Gao,
yuangao_sar@cumt.edu.cn;
y.gao3@leeds.ac.uk

Citation:

Gao, Y., Ou, Q., Fang, J., Carpenter, M., Wright, T. J., Allison, K., et al. (2026). Geodetic constraints on fault kinematics and dynamics of 2021 Maduo earthquake: Implications for fault friction. *Journal of Geophysical Research: Solid Earth*, *131*, e2025JB033035. https://doi.org/10.1029/2025JB033035

Received 4 OCT 2025
Accepted 29 JUN 2026

Author Contributions:

Conceptualization: Qi Ou, Tim J. Wright
Data curation: Yuan Gao
Formal analysis: Manon Carpenter, Zhong Lu
Funding acquisition: Yuan Gao, Tim J. Wright, Wei Qu, Qin Zhang, Zhong Lu
Investigation: Tim J. Wright
Methodology: Yuan Gao, Qi Ou, Jin Fang, Kali Allison
Software: Yuan Gao, Qi Ou, Manon Carpenter, Kali Allison, Milan Lazecký, Yasser Maghsoudi
Supervision: Tim J. Wright, Wei Qu, Qin Zhang, Zhong Lu
Validation: Yuan Gao, Jin Fang
Visualization: Yuan Gao

Abstract Postseismic afterslip has been inferred to occur on fault barriers surrounding coseismic asperities, which can be explained by velocity-strengthening friction in barriers and velocity-weakening friction in asperities. However, afterslip also exhibits spatial overlap with coseismic slip for some events. Here we use ∼2 years of Sentinel-1 interferometric synthetic aperture radar (InSAR) data to study the postseismic deformation following the 2021 Mw 7.4 Maduo earthquake. Additionally, we use ∼7 years of InSAR data to generate the interseismic velocity and remove the interseismic contributions from postseismic data. We observe localized postseismic creep in the middle segment of the seismogenic fault, and distributed deformation in far field. We first apply a kinematic inversion to model the afterslip and find significant overlap between afterslip and coseismic slip on fault shallow region. We then conduct dynamic earthquake cycle simulations with vertical variations of friction to understand the conditions required for this to occur. Numerical models suggest that shallow part with velocity-strengthening properties can rupture seismically and creep during postseismic and interseismic periods. Our dynamic model partially explains the overlapping slip of the Maduo earthquake. However, the required shallow interseismic creep is not seen through detailed analysis of the interseismic velocity, implying that creep is either absent or too low to be observed. Our work enhances the understanding of fault friction control on fault slip during the earthquake cycle.

Plain Language Summary Slow slip after an earthquake, called afterslip, often occurs on fault areas that did not slip during the earthquake. This can be explained by differences in frictional properties of different parts of the fault: some parts resist the sliding while others in favor of. However, in some cases, afterslip has been inferred to occur in the same areas that slipped during the earthquake. In this study, we used about 2 years of satellite data to look at the fault movements after the 2021 Mw 7.4 Maduo earthquake. We also used 7 years of satellite data to measure the deformation before this earthquake. We found that afterslip overlapped with the areas that slipped during the earthquake. To understand why this happens, we ran numerical simulations to investigate how the fault deforms over time, based on different friction properties at various depths. The model showed that shallow fault areas with the property of resisting sliding can rupture during an earthquake and creep afterward. Such property would also promote the fault to creep before the earthquake. However, we do not find any pre-earthquake creep, suggesting that either there is no creep or it is too small to detect.

1. Introduction

Understanding the mechanisms of seismic and aseismic slip is crucial for elucidating the physics governing fault slip behaviors. Laboratory experiments on rock friction of earthquake faults have developed the constitutive relations of rate- and state-dependent friction theory (Dieterich & Kilgore, 1994; Dieterich, 1978; Marone, 1998; Marone et al., 1991; Ruina, 1983). In this framework, earthquake ruptures occur on velocity-weakening asperities, where frictional resistance decreases as slip velocity increases. Afterslip has been inferred to take place on fault barriers surrounding coseismic asperities (Marone, 1998; Marone et al., 1991). The barriers, which resist sliding as slip velocity increases and are characterized as velocity-strengthening, can promote earthquake arrest and lead to stable aseismic slip. For example, postseismic slip of the 2017 Mw 7.3 Sarpol-e Zahab earthquake

Writing – original draft: Yuan Gao
Writing – review & editing: Qi Ou, Jin Fang, Manon Carpenter, Tim J. Wright, Kali Allison, Wei Qu, Qin Zhang, Milan Lazecký, Yasser Maghsoudi, Zhong Lu

spatially complemented the coseismic slip, suggesting that coseismic stress change promoted ongoing afterslip on the fault barriers (Wang & Bürgmann, 2020).

However, in some events, despite the inherent uncertainties in inversion modeling, afterslip unambiguously exhibits spatial overlap with coseismic slip, such as the 2011 Mw 9.0 Tohoku, 2015 Mw 8.3 Illapel and 2003 Mw 6.8 Chengkung earthquakes (Barnhart et al., 2016; Johnson et al., 2012; Meade, 2024; Thomas et al., 2017). In particular, Johnson et al. (2012) pointed out that exclusion of asperities in afterslip modeling does not allow them to fit postseismic observations of 2011 Mw 9.0 Tohoku-oki earthquake. Mechanisms responsible for such overlapping slip remain unclear. One possible explanation is that fault friction may transform from velocity-weakening to velocity-strengthening as a result of possible fluid injection or shear heating after an earthquake (Bedford et al., 2013; Thomas et al., 2017); the reduction of effective normal stress due to elevated pore fluid pressure, can facilitate afterslip in areas where coseismic slip has occurred (Bedford et al., 2013; Dalaison et al., 2021). Numerical models also suggest that shear heating can significantly increase the temperature, transforming velocity-weakening friction into velocity-strengthening, thereby leading to afterslip in areas with coseismic slip (Thomas et al., 2017). In these scenarios, fault remains locked before the earthquake, and releases slip deficit during coseismic and postseismic periods.

Alternatively, the frictional properties of the afterslip areas on a fault may be velocity strengthening throughout the earthquake cycle, leading to the expectation of fault creep before the earthquake (Kaneko et al., 2013; Lindsey & Fialko, 2016). The velocity-strengthening friction and low strength of the unconsolidated uppermost crust is supported by laboratory experiment on granite (Blanpied et al., 1991). This hypothesis is also supported by geodetic observations on the western North Anatolian Fault where shallow slip both before and after the 1999 Izmit earthquake was observed in fault patches overlapping with the coseismic slip (Hussain et al., 2016). Fault segments with velocity-strengthening properties can also rupture seismically due to dynamic weakening (Noda & Lapusta, 2013). Both the 1999 Mw 7.6 Chi-Chi and 2011 Mw 9.0 Tohoku-Oki earthquakes exhibited large seismic slip in creeping areas that was considered stable (Noda & Lapusta, 2013; Tanikawa & Shimamoto, 2009).

Given diverse slip patterns associated with different fault friction regimes, it is important to understand fault slip behavior across different earthquake stages. Geodetic observations enable us to probe how fault slips during different stages of the earthquake cycle. Numerical modeling incorporating rate- and state-dependent friction has successfully reproduced earthquake cycles (Barbot et al., 2009; Erickson et al., 2020; Jiang et al., 2022; Lapusta et al., 2000; Lapusta & Rice, 2003) and has provided fruitful insights into mechanisms for different fault slip behaviors, including fluid-induced rupture in creeping areas (Noda & Lapusta, 2013), pore pressure evolution during seismic and aseismic sequences (Zhu et al., 2020), the influence of shear heating (Allison & Dunham, 2021), and seismic or aseismic slip in velocity-weakening region (Molina-Ormazabal et al., 2023). Using geodetic observations as constraints for earthquake cycle simulations enables us to infer possible in situ frictional properties (Kaneko et al., 2013; Lindsey & Fialko, 2016; Wei et al., 2013).

For velocity-strengthening regime in shallow fault areas, long-term creep may take up a considerable proportion of the commonly observed shallow slip deficit (Fialko et al., 2005; Kaneko & Fialko, 2011). Whereas postseismic slip, off-fault and inelastic deformation and inclusion of layered elastic half space may compensate for part of the slip deficit (Fialko et al., 2005; Jin et al., 2022; Marchandon et al., 2021), cumulative slip from interseismic creep in the shallow velocity-strengthening layer can be large, given hundreds to thousands years of recurrence interval for large earthquakes. Under different friction conditions, dynamic earthquake cycle simulations provide insight into how much slip is caused by interseismic creep, especially in areas where creep rates are below the detection capacity of geodetic observations (Kaneko & Fialko, 2011).

The 2021 Mw 7.4 Maduo earthquake occurred in the interior of Bayan Har Block in eastern Tibetan Plateau. This earthquake ruptured ∼150 km of the Jiangcuo Fault, previously a poorly-known sinistral strike-slip fault (Pan et al., 2022). This earthquake provides us with a chance to understand fault friction behavior during an earthquake cycle, as we have dense time series of InSAR observations before and after the earthquake.

Here we use ∼2 years of Sentinel-1 InSAR data to study postseismic deformation following the Maduo earthquake. Additionally, we use ∼7 years of InSAR data to generate the interseismic velocity. We remove interseismic contributions and long-wavelength noise in postseismic data using interseismic velocity through transforming both data into Eurasian reference frame. We apply a kinematic inversion to model the afterslip and find that significant afterslip occurred on shallow fault region that also slipped coseismically. We then model the

10.1029/2025JB033035

earthquake cycle slip using numerical simulations incorporating vertical variations of friction to understand the mechanisms causing such overlap. Our model shows that a shallow velocity-weakening layer locks immediately after an earthquake, while a velocity-strengthening layer can rupture and creep during postseismic and interseismic periods. Through comprehensive analysis of interseismic strain rate and slip rate, we do not observe clear strain localization or fault creep across the Jiangcuo Fault. We speculate that the creep is either not observed, or is obscured by noise in our data.

2. InSAR Data Processing and Time Series Inversion

We independently process the interseismic and postseismic InSAR time series, rather than constructing a continuous time series spanning the full earthquake cycle, to minimize phase-unwrapping errors and coherence loss near the fault caused by large coseismic slip gradients. The contribution of deformation from neighboring faults is removed from the postseismic displacement field using the interseismic velocity field.

2.1. Interseismic Data

We use the COMET-LiCSAR system (Lazecký et al., 2020) to generate ∼7 years of interferograms for 7 descending frames and 9 ascending frames acquired from October 2014 to the last epoch before the 22 May 2021 Maduo earthquake. We remove 6 and 12 days of interferograms to reduce potential phase bias (Ansari et al., 2021). We additionally generate interferograms with temporal baselines between 180 and 360 days to improve the signal-to-noise ratio (Figure S1 in Supporting Information S1). All interferograms are multilooked into 100 m resolution and unwrapped by the Statistical-Cost, Network-Flow Algorithm for Phase Unwrapping (SNAPHU) method (Chen & Zebker, 2002). We then use the LiCSBAS algorithm (Morishita et al., 2020) to invert for the InSAR time series. The interferograms are multilooked to a 500 m resolution to improve processing efficiency and to apply reunwrapping, which increases the data reliability and spatial coverage. The reunwrapping method has been routinely applied to the COMET-LiCSAR system, and further details are provided in Lazecký et al. (2022). The Generic Atmospheric Correction Online Service (GACOS) model is used to reduce the atmospheric noise in each interferogram (Yu et al., 2018).We mask the time series using a suite of parameters to rule out the data with poor quality (Table S1 in Supporting Information S1). We perform the joint inversion of the linear velocity and seasonal oscillation of each pixel by a weighted least square method. We use bootstrapping with 100 iterations to estimate the standard deviation of the velocities.

2.1.1. Plate Motion Correction and Frame Stitching

The velocity map shows a long-wavelength ramp along range direction (Figure S2 in Supporting Information S1). Stephenson et al. (2022) suggested that rigid plate motion is a dominating contribution to such signals. For each frame, we project plate motion caused by rotation of the Eurasian Plate into InSAR line-of-sight (LOS) directions and transform the results into InSAR interior reference. Profiles of plate motion along range direction shows slight curvature, which is not suitable to be removed by a planar ramp (Figure S3b in Supporting Information S1). After subtracting plate motion fraction, the velocity map is flattened along range direction (Figure S4 in Supporting Information S1). Since each InSAR velocity frame is referenced to a local reference point, a constant offset exists between frames within each track. Offsets across tracks are caused by changing incidence angles.

To generate a large-scale velocity map, we need to tranform the multi-track InSAR velocities into a common reference frame. We tie all InSAR velocity map into the GNSS reference frame by fitting a planar ramp using both difference between InSAR and GNSS LOS velocity and offset between two overlapping frames along tracks, following the methods proposed by Shen et al. (2024) and Ou et al. (2022) (Figure S5 in Supporting Information S1). This step also reduces the residual long-wavelength noise, which primarily caused by ionospheric phase, and also orbital errors and solid Earth tide (Lemrabet et al., 2023). After applying the GNSS-based correction, the difference between the InSAR and GNSS LOS velocity follows a normal distribution with a mode of less than 0.7 mm/yr and a standard deviation of 2.0 mm/yr (Figure S6 in Supporting Information S1).

We only use horizontal GNSS velocity for referencing, since it is more accurate and is also one-order larger than vertical deformation in eastern Tibetan Plateau (Liang et al., 2013; Wang & Shen, 2020; Zhao et al., 2023; Zheng et al., 2017). InSAR captures surface movement from tectonic deformation and nontectonic signal from sedimentary erosion, permafrost, hydrology and anthropology (Lemrabet et al., 2023; Ou et al., 2022). These nontectonic activity can lead to short spatial wavelength variability in vertical movement (Ou et al., 2022).

While our InSAR processing follows a GNSS-tied referencing strategy consistent with previous studies (e.g., Ou et al., 2022), we acknowledge the evolving capability of Sentinel-1 to resolve long-wavelength signals independently. Liu et al. (2025) demonstrates that with rigorous correction of tropospheric, ionospheric and solid Earth tide noise, InSAR can robustly capture large-scale deformation rates. Achieving this level of independence globally requires highly precise correction models. While the GNSS network in the Maduo region provides a stable datum, future studies using these "GNSS-free" techniques may offer further insights into the large-scale velocity field analysis.

2.1.2. Velocity Decomposition

The stitched InSAR velocity no longer shows discontinuity along track (Figure S7 in Supporting Information S1). The remaining issue is discontinuity across tracks due to different incidence angles, which can be further reduced after decomposition into E-W and vertical velocities (Wright et al., 2004). We use InSAR LOS uncertainty to weight the decomposition. Uncertainties of InSAR velocity gradually increase with distance to the selected reference point. To remove such artifact caused by selection of reference point, we fit a spherical model of uncertainty profile against distance to reference point of each frame. We then scale up the profile by multiplying each uncertainty value by the ratio between the modeled sill and spherical model (Figure S8 in Supporting Information S1) (Ou et al., 2022).

We interpolate the north velocity (V_N) of GNSS data into InSAR resolution using an adjustable tension continuous curvature splines method (Smith & Wessel, 1990) (Figure S9 in Supporting Information S1). This method interpolates data to a minimum-curvature surface with continuous second derivatives and eliminate large oscillations by adding a tension parameter (Smith & Wessel, 1990). We assume the interpolated V_N is correct and decompose the ascending and descending velocity map into east (V_E) and vertical velocity (V_U) components (Figures 1a and 1b) (Hussain et al., 2018; Weiss et al., 2020; Wright et al., 2004), and estimate their uncertainties (Figure S10 in Supporting Information S1) (Ou et al., 2022).

InSAR V_E shows clear velocity gradient in short-wavelength across faults, especially on the East Kunlun Fault, while the broad regional motion is anchored by the GNSS network. Linear fitting between InSAR and GNSS V_E has a gradient of 0.96 and R^2 of 0.95 (Figure 1c). Comparing with previous work that uses short temporal baselines, our InSAR V_E has denser data coverage and less topography-correlated signal in short-wavelength (Figure S11 in Supporting Information S1) (e.g., Fang et al., 2022). We also see small scale vertical movement with high order of spatial variation, and poor correlation between InSAR and GNSS V_U with a gradient of 0.02 and R^2 of 0.00 (Figure 1d). InSAR captures surface deformation while GNSS stations installed on bedrock in Tibetan Plateau aim to monitor tectonic deformation. Two techniques may capture different source of vertical signals at some points, which leads to poor correlation in vertical component.

2.2. Postseismic Data

We repeat the data processing chain to generate interferograms and invert for LOS displacement time series of 2 descending and 2 ascending frames for postseismic deformation analysis. Data acquisitions are from the first epoch after the earthquake to 04 April 2023. We mosaic wrapped interferograms along track before unwrapping so that the interferometric network of consecutive frames is consistent (Figure S12 in Supporting Information S1) (Fang et al., 2022). We observe a long-wavelength ramp from cumulative LOS displacement (Figure S13 in Supporting Information S1), which is not straightforwardly compensated by a plate motion model (Figures S14a and S15a in Supporting Information S1). In addition, in tectonically active Tibetan Plateau, 2 years of observation not only includes postseismic deformation of the Maduo earthquake, but also includes contributions from interseismic movement on neighboring faults and nearby blocks. We exclude any such time-invariant contributions using the interseismic velocity map.

2.2.1. Correction for Long-Wavelength Noise

Due to the limited availability of concurrent GNSS time series, the postseismic InSAR data is referenced to the far-field interseismic InSAR velocity. We assume the region outside the postseismic movement area still deforms interseismically and linearly with time. Hence, we treat the difference between far-field postseismic and the interseismic LOS displacements as the difference between two reference frames and unmodeled long-wavelength noises in the postseismic data (Figure S14c in Supporting Information S1). For each epoch of the cumulative

10.1029/2025JB033035

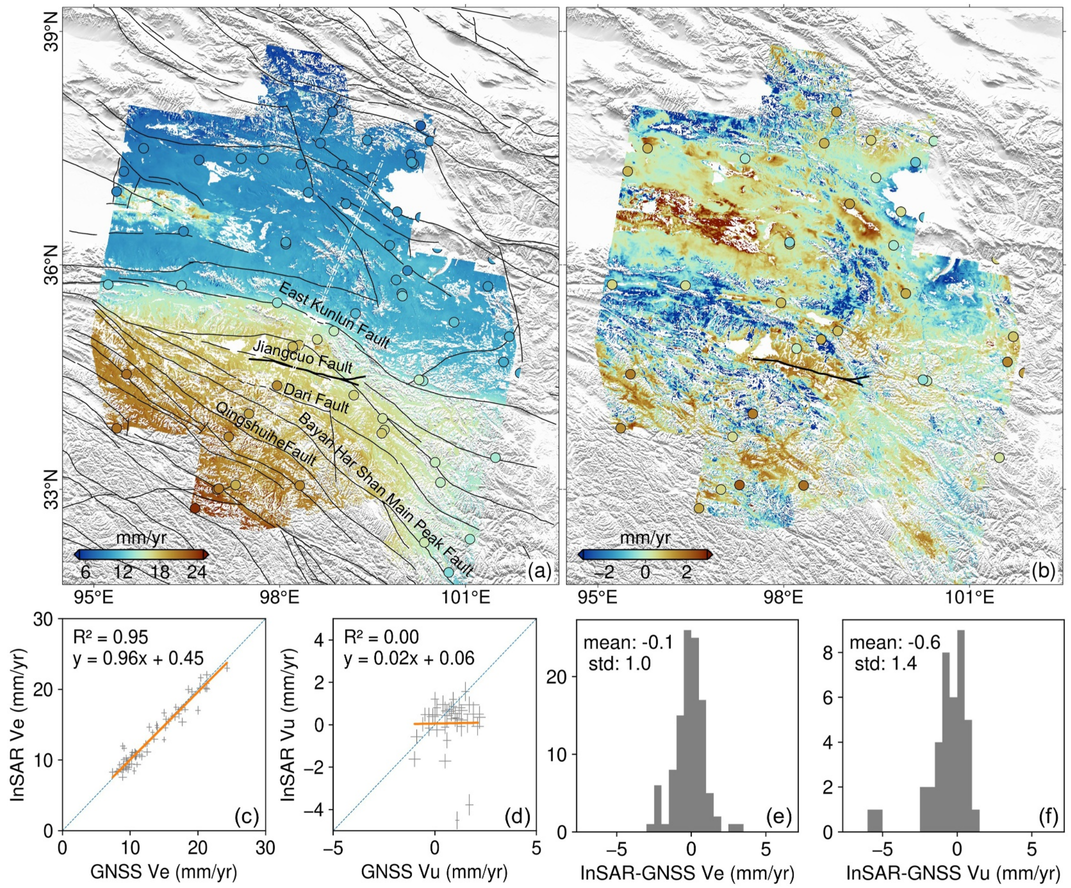

Figure 1. (a) Interseismic east and (b) vertical velocity (positive value is up and negative value is down) decomposed from descending and ascending InSAR line-of-sight velocity. Colored circles represent horizontal (a) (Wang & Shen, 2020) and vertical (b) GNSS velocities (Zhao et al., 2023). Thick black lines mark the Jiangcuo Fault and thin black lines mark surrounding faults. (c) Correlation analysis between InSAR and GNSS V_E. Gray crosses represent InSAR and GNSS data with uncertainties. The blue dashed line is a reference line with slope of 1. Orange line represents weighted best-fit linear regression model. (e) Histogram of difference between InSAR and GNSS V_E. (d, f) Analogous to (c, e) but for InSAR and GNSS V_U.

postseismic displacement, we calculate the corresponding interseismic displacement, and mask their difference near the Jiangcuo Fault with a polygon (300 × 180 km, see Figure S14c in Supporting Information S1). We invert for a first-order planar ramp from the far-field difference between the postseismic and interseismic LOS displacements, and subtract the ramp from the postseismic displacement (Figures S14 and S15 in Supporting Information S1). This step effectively places the postseismic displacements in the same reference frame as the interseismic velocities and remove any long-wavelength noise present in the postseismic displacement time series. Take the final epoch 20230404 as an example, we observe notable long-wavelength ramp, especially from the ascending track. The standard deviation of the far-field difference between the interseismic and postseismic displacements reduces from 30.9 to 10.6 mm for the ascending track (Figures S14g and S14h in Supporting Information S1) and 12.2–10.2 mm for the descending track (Figures S15g and S15h in Supporting Information S1). We test different far-field polygon sizes for the ramp estimation and found that the resulting influence on the ramp model is negligible (Figure S16 in Supporting Information S1). While polynomial detrending effectively isolates the transient postseismic displacment, we acknowledge that it may also suppress long-wavelength signals associated with deep-seated postseismic processes (such as deep viscoelastic relaxation).

2.2.2. Removal of Interseismic Component

Since we use more conservative parameter thresholds to mask interseismic velocity than postseismic data (Tables S1 and S2 in Supporting Information S1), the interseismic data has fewer pixels. Directly subtracting interseismic

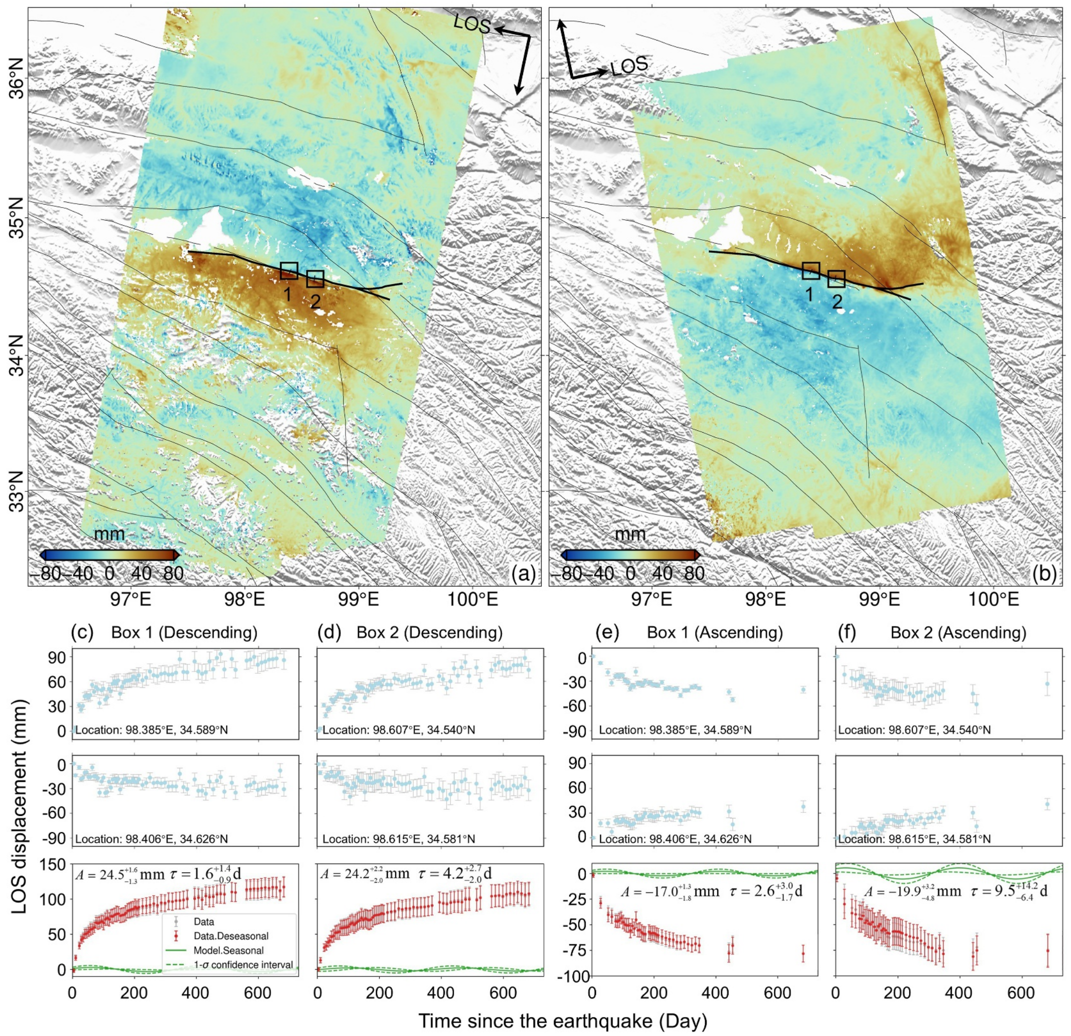

Figure 2. Cumulative line-of-sight postseismic displacement from 26 May 2021 to 04 April 2023 for both descending (a) and ascending (b) tracks after removing a planar ramp and the interseismic contribution. Pixels with cold color move away from the satellite and pixels with warm color move toward the satellite. Black arrow labeled with "LOS" represents line-of-sight direction and the other perpendicular arrow represents satellite flight direction. The thick black line represents the location of Jiangcuo Fault and the thin black lines represent other faults. Two boxes labeled with 1 and 2 are used for time series analysis. (c) Time series of displacement (light blue with gray cap) of two points located in each side of the fault in box 1 from descending data. Gray and red vertical bars with cap represent time series of displacement by calculating data difference of the two points in box 1 before and after subtracting a seasonal model. We sample two points located approximately 2 km to the fault on both sides and calculate corresponding mean value of 10 pixels closest to each point. Green solid and dash line represent seasonal model and 1-σ uncertainty. (d) Analogous to (c) but for data in Box 2. (e, f) Analogous to (c, d) but for the ascending data.

component with interseismic velocity map leads to pixel loss from the postseismic data, including the region near the Jiangcuo Fault, which holds key information for the postseismic evolution that we want to investigate. Therefore, we project the median filtered InSAR V_E and interpolated GNSS V_N to produce LOS displacements with full coverage (Figures S14b and S15b in Supporting Information S1) and then subtract them from the postseismic displacements in the LOS. V_U is not used there as it primarily consists of short-wavelength non-tectonic signals that are not necessarily time invariant(Daout et al., 2020). After removing long-wavelength ramp and interseismic components, we observe a discontinuity across the Jiangcuo fault (Figures 2a and 2b). The most clear postseismic afterslip is in fault middle segment from 98.1°E to 98.7°E, which can be interpreted as shallow afterslip. We also see distributed long-wavelength signal in far field resultant from either deep afterslip or viscoelastic relaxation (e.g., Chen et al., 2024; Jin et al., 2023; Li et al., 2025).

Near-fault displacement time series exhibits notable decay. Taking the difference between two neighboring pixel groups across the fault helps suppress spatially correlated noise. These time serie are the results of mixed signals including seasonal signal, transient postseismic deformation and noise. We assume a logarithmic decay of postseismic deformation (Marone et al., 1991) and sinusoidal terms (Ingleby et al., 2020) for seasonal signals. We therefore use the following function to extract the postseismic signal:

$$y = A\ln\left(1 + \frac{t}{\tau}\right) + B\sin(2\pi t) + C\cos(2\pi t) + D \tag{1}$$

where A is a scaling constant for logarithmic decay, τ is a relaxation time, t is time after the earthquake, B and C are scaling constants for sinusoidal terms, D is an offset. We select two areas in fault middle segment with clear creep to analyze their slip mode. A Bayesian inversion approach (Goodman & Weare, 2010) is used to calculate the acceptable range for each unknown parameter. The amplitude of the sinusoidal signal for both descending and ascending data is much smaller, comparing to the total slip (Figures 2c–2f). The marginal probability distributions for each parameter (Figures S17 and S18 in Supporting Information S1) indicate that the posterior distributions are approximately Gaussian. A notable exception is the relaxation time τ, which clusters near the lower bound of the prior range.

We compare the postseismic deformation field with the published coseismic field (Figure S19 in Supporting Information S1) (Chen et al., 2022; Fang et al., 2022; Xu et al., 2023). The coseismic slip profiles show clear discontinuities across the fault, suggesting that the earthquake ruptured to the surface, consistent with field observations (Pan et al., 2022). In the middle segment of the fault, the postseismic slip profiles also reveal notable shallow creep, implying that these regions continued to slip after the earthquake. Accordingly, we perform kinematic afterslip inversions in the following section to compare the spatial distribution with the coseismic slip model.

3. Kinematic Model of Postseismic Slip

3.1. Afterslip Model

Kinematic afterslip models derived from surface deformation and dislocation theory enable us to resolve slip distribution on a fault plane. Fang et al. (2022) derived coseismic slip and early afterslip models (up to 6 months) of Maduo earthquake using the same approach. Following their work we use the same fault configuration to derive a reference afterslip model. We also derive another model including one more deep fault layer to fit the far-field observation. We note that slip on deep fault may be overestimated, as both deep afterslip and viscoelastic relaxation in the lower crust and upper mantle produce similar surface deformation in spatial and temporal pattern associated with strike-slip events (Barker, 1976; Savage, 1990).

3.1.1. Model Configuration

We adopt the fault geometry constructed by Fang et al. (2022) from the rupture trace from coseismic SAR range offsets, including a branching fault in the southern end. The fault is divided into 13 segments along strike, and each segment has a fixed strike angle. The dip angle of each segment is constrained by 8 days of relocated aftershocks (Wang et al., 2021). The down-dip patch size is adjusted based on model resolution and each segment is then discretized into patches that are approximately square. Given poor resolution of deep slip constrained by surface observations, the fault was divided into four layers with increasing size through depth: 0–1 km, 1–4 km, 4–10 km, and 10–20 km. We also test one model with an additional layer in the depth range 20–35 km.

Both ascending and descending LOS cumulative displacement are used as geodetic constraints. To quantify the spatially correlated noise before inversion, we calculate a variance-covariance matrix using an exponential function by computing a semivariogram with data located in an "undeforming" region (Bagnardi & Hooper, 2018). The modeled sill of 10^{-5}–10^{-4} m^2, nugget of 10^{-5} m^2 and range of $>$ 10 km in magnitude, are used as input parameters. We find that selecting data from 'non-deforming' regions does alter these parameters but has little influence on the inferred slip distribution. For model efficiency, we downsample the data with a nested uniform approach with different sampling intervals in difference regions. We resample the data every 4 pixels in the near fault area to keep the short wavelength signal, and every 8 and 16 pixels in middle- and far-field fault areas (see Figure S20 in Supporting Information S1). Pixels located very close to or overlapping the fault trace are

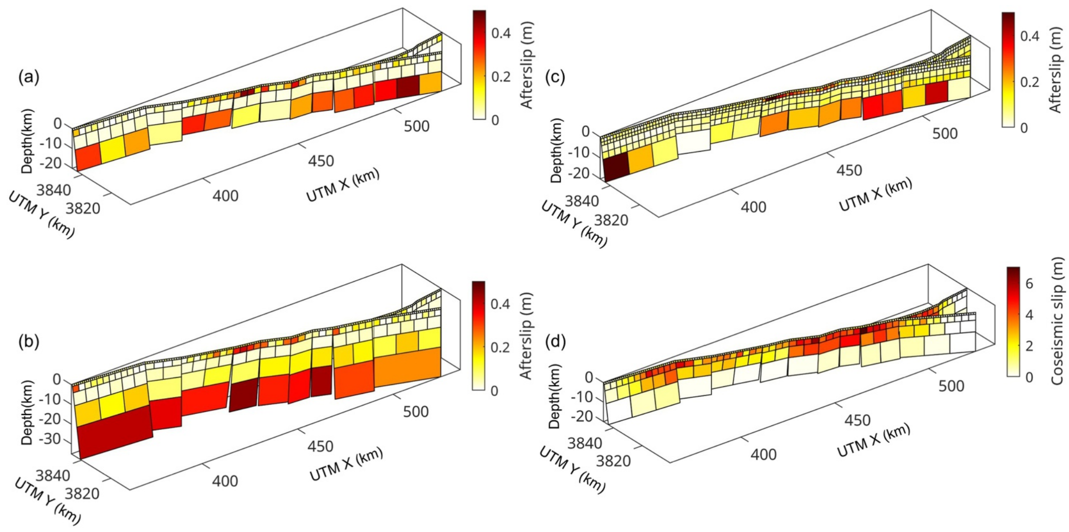

Figure 3. (a) Afterslip model derived from cumulative postseismic displacement at epoch 20230404 (23 months after the earthquake). (b) Analogous to (a) but with one additional fault layer in 20–35 km depth. (c) Analogous to (a) but with smaller patches sizes in 0–10 km depth. (d) Coseimsic slip model from Fang et al. (2022).

retained. We acknowledge that averaging signals from both sides of the fault may reduce the displacement gradient (Wang et al., 2024). Our model would be interpreted as conservative estimate of the shallow afterslip.

We invert for the slip vector of each patch using the slipBERI program which uses Markov chain Monte Carlo (MCMC) algorithm for inversion (Amey et al., 2018). We use the von Karman approach, a fractal spatial smoothing method, for regularization. This method has been shown in synthetic tests to provide more reliable confidence bounds for fault slip compared to Laplacian smoothing (Amey et al., 2018). We employ a hyperparameter to control the slip variance for each fault strand, and we find that the model is sensitive to this parameter's initialization. To ensure optimal sampling, if the MCMC rejection rate is excessively high, we take the searched hyperparameter values as a prior for a subsequent inversion. The initial slip is set to 0.2 m and the maximum slip is set to 0.8 m. The step size is initially set to 0.001 and can be adaptively adjusted through the iteration. We run the inversion for 400,000 iterations and remove the first 20,000 iteration as burn-in. We calculate the resolution matrix to quantify how robustly the data constrain the model.

3.1.2. Model Results

We derive both shallow and deep afterslip, as reflected by near fault creep and far-field deformation (Figures 3a and 3b). Shallow afterslip is up to 0.4 m and deep afterslip is up to 0.6 m. Slip at 4–10 km depth is less than 0.05 m, which is consistent with early afterslip model from Fang et al. (2022) in its spatial pattern. Models incorporating a deep fault layer yield root mean square (RMS) values of 10.9 and 14.3 mm for ascending and descending tracks, respectively, compared to RMS values of 12.0 and 16.0 mm for the model without a deep fault layer (Figures S20 and S21 in Supporting Information S1). The largest discrepancies occur at distances of 20–40 km from the fault trace. These far-field residuals may arise from distributed viscous flow in the lower crust/upper mantle or from unmodeled complexities in the fault geometry at depth (Jin et al., 2023; Li et al., 2025). We find that near-fault deformation is well-resolved by both models, where the standard deviations of afterslip of these patches are less than 0.06 m. Patch resolutions in the shallow layers exceed 0.7 (Figures S22 and S23 in Supporting Information S1), suggesting that the core features of the afterslip distribution are statistically robust.

Comparing two afterslip models we observe trade-off between afterslip at depth of 10–20 km and 20–35 km. Deep slip distribution is hard to robustly resolve due to low resolution in depth based on surface observations (Lohman & Simons, 2005). Moreover, distinguishing whether far-field deformation arises from deep afterslip or viscoelastic relaxation is challenging, as both processes can produce similar surface deformation in spatial and temporal domain (Barker, 1976; Savage, 1990). Li et al. (2025) suggests that, 2 years after the Maduo earthquake, afterslip primarily contributes to surface displacement within ~50 km of the fault, whereas viscoelastic relaxation dominates far-field deformation over a broader spatial extent. Despite the trade-off in the deeper layers, we have robust afterslip results in the shallower layers.

To evaluate the influence of discretization and regularization, we conduct inversions using smaller patch sizes in 0–10 km depth: 0–1.0 km, 1.0–2.5 km, 2.5–4.0 km, 4.0–7.0 km, and 7.0–10.0 km. We also compare our results against model using Laplacian regularization. While the model with smaller patch sizes indicates a higher-magnitude shallow afterslip concentrated at 1.0–2.5 km depth along the central fault segment (Figure 3c), the RMS of residuals is relatively high and patch resolution for this highly discretized configuration frequently drops below 0.5 (Figures S24 and S25 in Supporting Information S1). Furthermore, significant shallow slip along the central fault segment is consistently resolved even when employing Laplacian regularization (Figures S26 in Supporting Information S1). Despite the variation in regularization schemes and the lower resolution of the smaller patches, all models reveal notable shallow afterslip in this region, confirming the robustness of the afterslip pattern.

3.2. Overlap Between Coseismic and Postseismic Models

We compare our afterslip models with previous published coseismic slip model (Figure 3d) (Fang et al., 2022). We find slip in 4–10 km depth of both afterslip models is lower that 0.1 m (Figures 3a and 3b), where coseismic slip is over 2.0 m. Afterslip in fault patches deeper than 10 km exceeds 0.1 m and is up to 0.5 m, where coseismic slip is lower than 1.0 m. These observations are consistent with the rate- and state-dependent friction law which states that earthquake ruptures velocity-weakening material and afterslip takes place in velocity-strengthening areas (Marone et al., 1991; Scholz, 1998). However, when we compare the coseismic and postseismic slip variation along fault strike in 0–1 km and 1–4 km depth respectively (Figure 4), we find significant afterslip on shallow fault segments between 98.1°E and 98.7°E that also slipped coseismically. Specifically, afterslip of 0.1–0.2 m occurred at depths of 0–1 km, compared to 0.5–2.5 m of coseismic slip, and afterslip of 0.1–0.4 m occurred at depths of 1–4 km, compared to 2.0–6.0 m of coseismic slip (Figure 4). While coseismic slip may be overestimated due to inclusion of 4 days of postseismic deformation, subtracting the early postseismic slip does not negate the presence of overlapping slip, because most surface coseismic slip in this area reaches up to 1.0 m (Fang et al., 2022), which is much larger than postseismic slip.

To test if the shallow afterslip is indispensable to account for the observation, we compare our models with those in which afterslip is not allowed to occurred in shallow areas (Johnson et al., 2012). To do so, we use the model with deep fault layer and remove layers at depths of 0–1 km, 1–4 km, and 0–4 km respectively, and perform inversions using the same procedure. The RMS of residuals increases when shallow fault geometry is excluded (Figures S27–S29 in Supporting Information S1). In particular, model without 0–4 km fault layer increases the RMS by 15% and 13% for both ascending and descending tracks and data near the fault is poorly fitted (Figure S29 in Supporting Information S1). For models without fault geometry at depths of 0–1 km or 1–4 km, afterslip redistributes on the other shallow layers (Figures S27 and S28 in Supporting Information S1). Hence, afterslip on coseismic rupture areas is required to fit the postseismic observations, which convinced us there is a spatial overlap between fault patches that slipped coseismic and postseismically.

Spatial overlap between postseismic and coseismic slip is not a unique case for the Maduo earthquake. Similar pattern have been found in the 2011 Mw 9.0 Tohoku (Johnson et al., 2012), 2015 Mw 8.3 Illapel (Barnhart et al., 2016), 2003 Mw 6.8 Chengkung (Thomas et al., 2017) and 2005 Mw 8.6 Nias-Simeulue (Qiu et al., 2019) earthquakes, as well as the 2016–2018 Chaman earthquake sequences (Dalaison et al., 2021). This slip behavior poses a challenge to classical stress-driven afterslip models which assume areas with state-strengthening friction is surrounding the velocity-weakening areas (Johnson et al., 2012; Meade, 2024).

4. Dynamic Earthquake Cycle Model

Kinematic models based on geodetic data enables us to understand slip distribution. However, these models provide little insight into fault's physical property responsible for such slip pattern. Numerical simulation is an alternative solution that uses physical laws governing friction and/or viscous flow to generate self-consistent fault stress and slip during multiple earthquake cycles (Allison & Dunham, 2018; Lapusta et al., 2000; Lapusta & Rice, 2003). We use numerical earthquake cycle simulation models incorporating variation of friction properties with depth to understand the condition causing spatial pattern of overlapping coseismic and postseismic slip (Allison & Dunham, 2018). We use the reference model based on Allison and Dunham (2018) with a velocity-

10.1029/2025JB033035

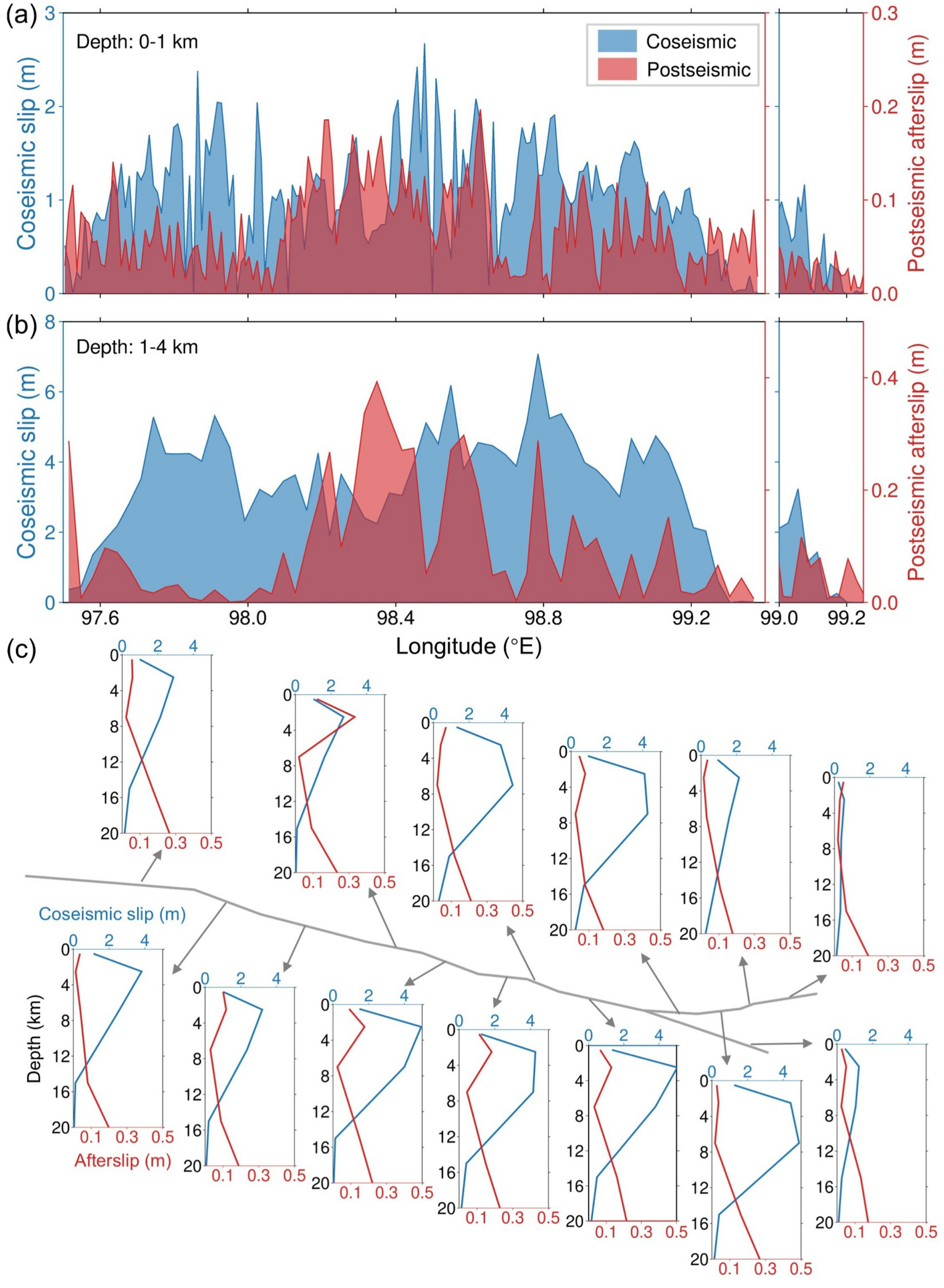

Figure 4. (a) Coseismic slip (blue) and afterslip (red) profile along strike direction in 0–1 km depth. Coseismic slip model is from Fang et al. (2022). Left panel represent slip in major fault and right panel represent slip in the branching fault in the south. (b) Analogous to (a) but for slip in 1–4 km depth. (c) Coseismic slip (blue) and afterslip (red) variations along depth by calculating the mean slip value plotted on the center depth of each layer of each fault segment pointed by a gray arrow. Gray line represent fault surface trace.

10.1029/2025JB033035

Table 1
Model Parameters for Earthquake Cycle Simulation

Parameter	Symbol	Value
Direct and state evolution effect	$(a-b)$	Depth variable, see Figures 5a, 5d, 5g, and 5j
Shallow velocity-strengthening thickness	T_{vs}	Variable (1–5 km)
Model length	L	500 km
Model width	W	500 km
Reference slip rate	V_0	10^{-6} m/s
Loading slip rate	V_l	1.0×10^{-9} m/s, 3.2×10^{-11} m/s
State evolution distance	D_c	30 mm, 15 mm, 5 mm
Reference friction coefficient for steady slip	f_0	0.6
Rock density	ρ	2700 kg/m^3
Hubbert-Rubey fluid pressure ratio	λ	0.37
Shear modulus	μ	30 GPa

weakening layer overriding on a velocity-strengthening layer. We also test another model with a shallow velocity-strengthening layer over a velocity-weakening layer, transmitting to deeper velocity-strengthening below the seismogenic upper crust. We test various friction properties at different depths and investigate slip partition during interseismic, coseismic, and postseismic periods to see if we can explain the spatial overlap between coseismic and postseismic slip revealed by our kinematic models.

4.1. Model Setup

We build a two-dimensional antiplane shear model with a vertical strike-slip fault embedded in a homogeneous elastic domain. We use a quasi-dynamic simulation for computational efficiency (Allison & Dunham, 2018). The material properties and remote tectonic loading are symmetric about the fault, allowing us to solve for stress and slip on one half of the domain. Antiplane displacement is governed by the static equilibrium equation and Hooke's law. The effective normal stress is equal to lithostatic pressure minus pore pressure. Pore pressure at depth is parameterized with the Hubbert-Rubey fluid pressure ratio λ, which is the ratio between pore pressure and lithostatic pressure (Allison & Dunham, 2018; Rubey & King Hubbert, 1959). Here we use $\lambda = 1{,}000\ \mathrm{kg/m^3}/2{,}700\ \mathrm{kg/m^3} \approx 0.37$ to represent the hydrostatic pore fluid pressure. A constant slip rate is applied to side boundaries below the seismogenic layer as remote tectonic loading. We apply a traction-free boundary condition at both surface and bottom of the domain. To minimize edge effects on simulation results, both the side and bottom boundaries are located 500 km away from the fault, which is consistent with previous model geometry used by Zhu et al. (2020) and Allison and Dunham (2021). Fault frictional strength is governed by rate-and-state friction law (Rice et al., 2001) and aging law for state variable (Marone, 1998; Ruina, 1983):

$$f(\psi, V) = a \sinh^{-1}\left(\frac{V}{2V_0} e^{\frac{\psi}{a}}\right) \tag{2}$$

$$G(\psi, V) = \frac{bV_0}{D_c}\left(e^{\frac{f_0-\psi}{b}} - \frac{V}{V_0}\right) \tag{3}$$

where f is the friction coefficient which determines the frictional strength, G is the rate of change of the state variable, ψ is the state variable representing a characteristic contact lifetime (Marone, 1998), V is the slip rate, a is rate parameter, V_0 is the reference slip rate, b is state parameter, D_c is the characteristic slip to renew surface contacts (Marone, 1998), f_0 is the constant friction for steady-state sliding at V_0. The constitutive parameter $(a-b)$ determines the fault frictional behavior at steady state. $(a-b) > 0$ leads to velocity-strengthening behavior, which resists sliding as slip velocity increase, leading to stable slip. On the other hand, $(a-b) < 0$ leads to velocity-weakening behavior, where frictional resistance decreases as slip velocity increases, potentially leading to unstable slip. Model geometry and parameters used in this study are shown in Table 1.

We use distributions of a and b along depth from sliding experiments on wet granite (Blanpied et al., 1991, 1995), which have been extensively used in earthquake cycle modeling (Allison & Dunham, 2021; Lapusta & Rice, 2003; Lapusta et al., 2000; Wei et al., 2013). Sliding experiments on wet granite show velocity-strengthening behavior at 23°C, 250°C and 350°C–600°C (Blanpied et al., 1991). Velocity-weakening behavior is observed at temperatures of 100°C–350°C except 250°C (Blanpied et al., 1991). The relationship between temperature and depth is inferred based on heat flow measurements (Lachenbruch & Sass, 1980). We use the reference model based on Allison and Dunham (2018) with a velocity-weakening layer overriding on a velocity-strengthening layer. We also have another model with a shallow velocity-strengthening layer on a velocity-weakening layer and transmitting to a deeper velocity-strengthening layer. Value of $(a - b)$ in deeper domain is linearly extrapolated based on linear dependence of a on temperature. We do not use any viscous rheology, as we focus on the friction properties of the shallow part of the fault, where fault strength predominantly exhibits brittle behavior. We use a finite difference method to discretize the governing equations (Allison & Dunham, 2018). To ensure accuracy and efficiency of numerical solution, we use small grid spacing in the vicinity of velocity-weakening layer and larger grid size elsewhere. More details about the spatial and temporal discretization of the numerical model can be found in Allison and Dunham (2018).

We first run the reference model, and a few models with a shallow velocity-strengthening layer with different values of $(a - b)$ and a fixed $T_{vs} = 4.0$ km, to analyze spatial patterns of fault slip in different earthquake stages. Although the shallow $(a - b)$ naturally varies along depth, we treat it as constant in each model as a first-order approximation. Coseismic slip is defined when slip velocity exceeds 1.0 mm/s (Allison & Dunham, 2018) and slip within 20 years of an earthquake is arbitrarily defined as postseismic. We then test other parameters including V_l and D_c to investigate their influence to the model. We finally fix the V_l and D_c, and conduct grid search to find the optimal combination of shallow $(a - b)$ and T_{vs}, using time series of postseismic slip as constraints. Earthquake cycle simulation needs to take a few numbers of earthquakes to spin-up and settles into a cycle-invariant state. We remove earthquake sequences before spin-up for analysis.

4.2. Model Results

4.2.1. Time Series of Slip Velocity Along Depth

For the reference model (Figure 5a), earthquake rupture occurs throughout the velocity-weakening domain and the coseismic slip reaches 16 m. The shallow part locks after coseismic rupture, and postseismic slip occurs in region below the seismogenic layer (Figure 5b). Cumulative interseismic creep in shallow region is less than 0.5 m (Figure 5c).

For models with a shallow velocity-strengthening layer, earthquake nucleates within the velocity-weakening area. However, coseismic slip propagates into velocity-strengthening areas, although with lower magnitude than the reference model (Figure 5c) leading to coseismic slip in this area. Afterslip takes place in both shallow and deep velocity-strengthening regions for model with $(a - b) = 0.0095$ (Figure 5e). There's a spatial overlap between coseismic and aseismic slip in the 0–4 km depth range (Figure 5f). The aseismic slip within this depth range includes both interseismic creep and postseismic slip. Fault slip in the 6–12 km depth is taken by coseismic rupture and no postseismic slip occurs in this region. This spatial pattern is in accordance with the results of kinematic model, despite significant difference in magnitude.

We experimented with two loading rates, V_l: one is 1.0×10^{-9}m/s, equivalent to 31.5 mm/yr, which is commonly used by earthquake cycle simulations (e.g., Allison & Dunham, 2021; Molina-Ormazabal et al., 2023; Noda & Lapusta, 2013; Wei et al., 2013). The other is 3.2×10^{-11}m/s, equivalent to 1.0 mm/yr, which represents estimate of fault slip rate on Jiangcuo Fault (Jian et al., 2022; Pan et al., 2022; Zhu et al., 2021). Coseismic slip generated by model with $V_l = 1.0$ mm/yr exceeds 15 m, even larger than coseismic slip generated by model with $V_l = 31.5$ mm/yr (Figures 5f and 5i). Both models produce similar overlap of coseismic and postseismic slip in the shallow part. The loading rates (V_l) do not necessarily have a big impact on depth distribution of slip but does influence the earthquake interval (Figures 5e and 5h). Recurrence interval shows a possible linear relationship with V_l. This may indicate that seismic moment release and earthquake potential is not strictly controlled by slip rate. Faults with relatively low slip rates can still accumulate sufficient strain to generate large earthquakes over longer timescales.

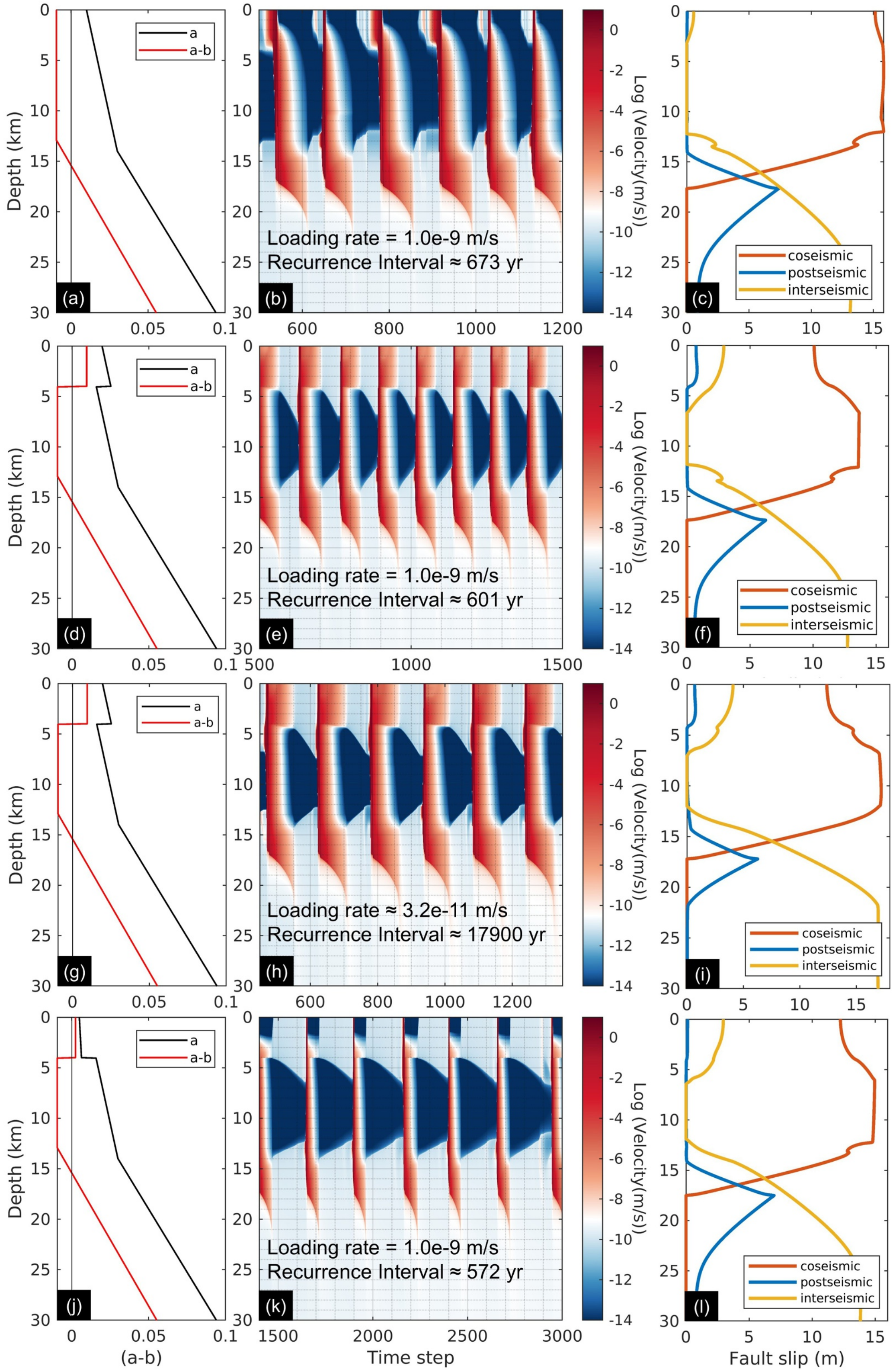

Depth (km)
a
a-b
(a)
(b)
(c)
Loading rate = 1.0e-9 m/s
Recurrence Interval ≈ 673 yr
Log (Velocity(m/s))
coseismic
postseismic
interseismic
(d)
(e)
(f)
Loading rate = 1.0e-9 m/s
Recurrence Interval ≈ 601 yr
(g)
(h)
(i)
Loading rate ≈ 3.2e-11 m/s
Recurrence Interval ≈ 17900 yr
(j)
(k)
(l)
Loading rate = 1.0e-9 m/s
Recurrence Interval ≈ 572 yr
(a-b)
Time step
Fault slip (m)

Figure 5.

If we make the shallow a-b infinitesimal (such as 0.0024) but still positive hence velocity strengthening, the earthquake still ruptures to the surface, but the shallow part locks immediately after the earthquake (Figures 5j and 5k). No clear overlap between coseismic and postseismic slip is observed in this model (Figure 5l). The slip velocity on the shallow part decreases to 10^{-12}m/s after an earthquake (Figure 5k), and increases to a steady stage. All models, even the reference model, generate interseismic creep in shallow part.

4.2.2. Model Test on D_c and V_l

Since there are more free parameters in the dynamic model than kinematic model, similar surface deformation can result from different combinations of parameters. We test different loading rates V_l and slip weakening distance D_c to investigate their influence on the model. Laboratory measurement suggest the D_c is within the range of 10^{-6}–10^{-5} mm (Marone, 1998; Scholz, 1988). However, D_c should be of magnitude of $\sim 10^{-2}$ mm to simulate a natural earthquake (Scholz, 1988). Such discrepancy arises from different size of fault zone widths in the laboratory and natural faults, since D_c scales with thickness of shear fault gouge (Marone, 1998; Marone & Kilgore, 1993; Scholz, 1988).

We test three different values of D_c (see Table 1) to investigate their effect on coseismic and postseismic slip. Reducing D_c significantly decreases the coseismic slip and slightly decrease the postseismic slip (Figure S30 in Supporting Information S1). Surface coseismic offset of Maduo earthquake based on geodetic observations is less than 3.0 m (Pan et al., 2022), which is smaller than the modeled 4.5 m with $D_c = 5$ mm. Using a smaller D_c may generate coseismic slip comparable to observations. However, a smaller D_c necessitates a much finer grid which greatly increases computational difficulty, as the grid size must be smaller than nucleation zone, which is approximately proportional to D_c (Lapusta & Rice, 2003). Since the impact of different D_c on postseismic slip is less significant than its effect on coseismic slip (Figures S30a and S30b in Supporting Information S1), we fix $D_c = 30$ mm in the following modeling for computational efficiency.

Models with different V_l yield similar amplitudes and temporal evolution of postseismic slip (Figures S31a and S31b in Supporting Information S1). Therefore, we fix $V_l = 31.5$ mm/yr in the following modeling.

4.2.3. Friction Property Constrained by Postseismic Data

We use time series of postseismic displacement from the Maduo earthquake to constrain friction parameters of the model (Figures 2c and 2e). Since the simulation is performed on one side of the fault, we multiply the simulation results by a factor of 2 to compare models with observed fault slip. We use time series of differential postseismic displacements across the fault from descending data as constraints since there is a data gap of 8 months for ascending data. We assume that postseismic LOS displacement is solely contributed by eastward movement, considering the near east-oriented strike-slip nature of the fault.

After fixing the V_l and D_c, we explore a range of different values of frictional parameters $(a - b)$ and layer thicknesses T_{vs}. We compare the data and model by extracting the time series of postseismic displacement from the last cycle's results at a node located 2 km from the fault. We reference the model to the time of the first InSAR acquisition by removing the slip that occurred before this time.

Our results show that increasing either $(a - b)$ or T_{vs} leads to larger amplitude of postseismic slip. The models reveal a strong trade-off between these two parameters (Figures 6 and 7), where a low T_{vs} requires a larger $(a - b)$ value to fit the time series of postseismic slip. In the model with $T_{vs} = 1.0$ km, the corresponding optimal $(a - b)$ for both data exceeds 0.05 (0.057 for data in Box 1 and 0.052 for data in Box 2) (Figure S32 in Supporting Information S1), larger than the range of 10^{-3}–10^{-2} estimated by laboratory experiments (Marone, 1998). For models with $T_{vs} = 2.0$ km or 3.0 km, optimal values of $(a - b)$ are within the range of 0.01–0.03 (Figures 6 and 7), which is at the upper end of the laboratory results (Marone, 1998). We found that for each $T_{vs} = 1.0$, 2.0 and

Figure 5. (a) Fault frictional property for reference model where a velocity-weakening layer overrides on a velocity-strengthening layer. (b) Modeled slip rate as a function of model time step. Loading rate is 1.0×10^{-9}m/s, equivalent to 31.5 mm/yr. Dark blue represents slip rate of 10^{-14}m/s, equivalent to 3.2×10^{-4}mm/yr, which can be regarded as fault locking. Dark red represents slip rate of over 1.0 m/s, which can be regarded as coseismic slip. (c) Cumulative interseismic, coseismic and postseismic slip along depth extracted from the last cycle results. (d–f) Analogous to (a–c) but includes a shallow velocity-strengthening layer where the $(a - b) = 0.0095$ and thickness is 4.0 km. (g–i) Analogous to (d–f) but with a loading rate of 3.2×10^{-11}mm/s, equivalent to 1.0 mm/yr. (j–l) Analogous to (d–f) except shallow $(a - b) = 0.0024$.

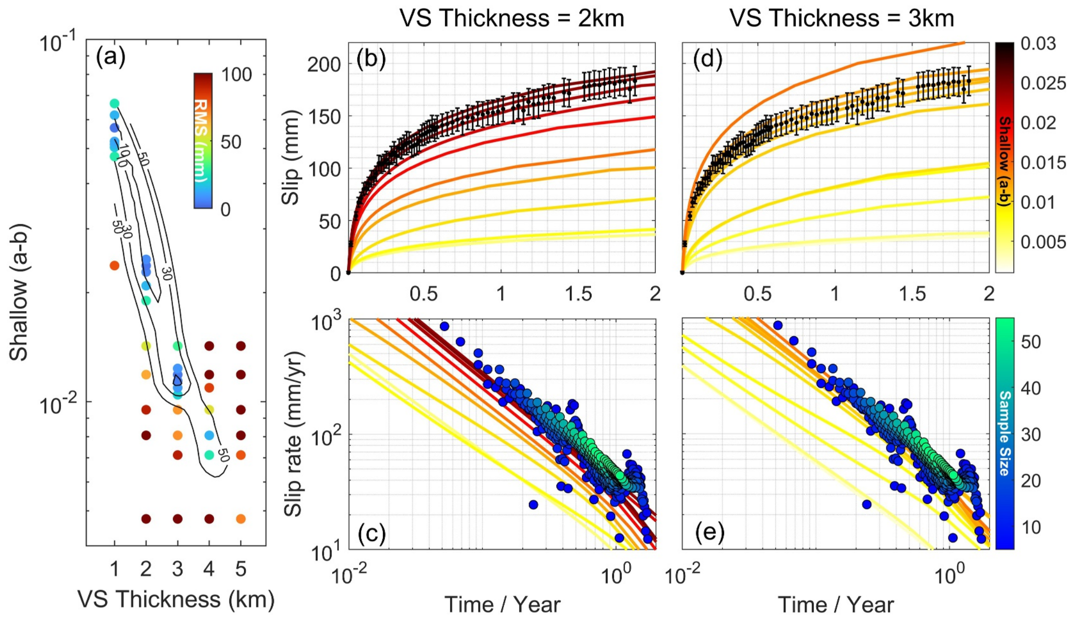

Figure 6. (a) Root mean square (RMS) misfit between observations in Box 1 shown in Figure 2 and modeled surface displacement for different combinations of $(a - b)$ and T_{vs}. Three black contour lines represent the 10 mm, 30 mm, and 50 mm RMS values, respectively. (b) Comparison between observed and modeled slip. Curve represents modeled time series of slip when $T_{vs} = 2.0$ km. Darker color represents results from larger $(a - b)$. Black bar with caps represents observed slip and uncertainty in Box 1. (c) Comparison between slip rate estimated by data and model. Curve represents slip rate estimated by model when $T_{vs} = 2.0$ km. Circles represent slip rate estimated by observations, with different color represent slip rate estimated by piecewise data fitting using various sample windows. Green color represent bigger window size. (d, e) Analogous to (b, c) but for $T_{vs} = 3.0$ km.

3.0 km, corresponding optimal $(a - b)$ can be found to reproduce the observed postseismic deformation. Modeled time series of slip no longer closely align with the data when $T_{vs} = 4.0$ km or higher (Figure S33 in Supporting Information S1). We speculate that thickness of shallow velocity-strengthening layer is less than 4.0 km, based on our observations and combinations of model parameters.

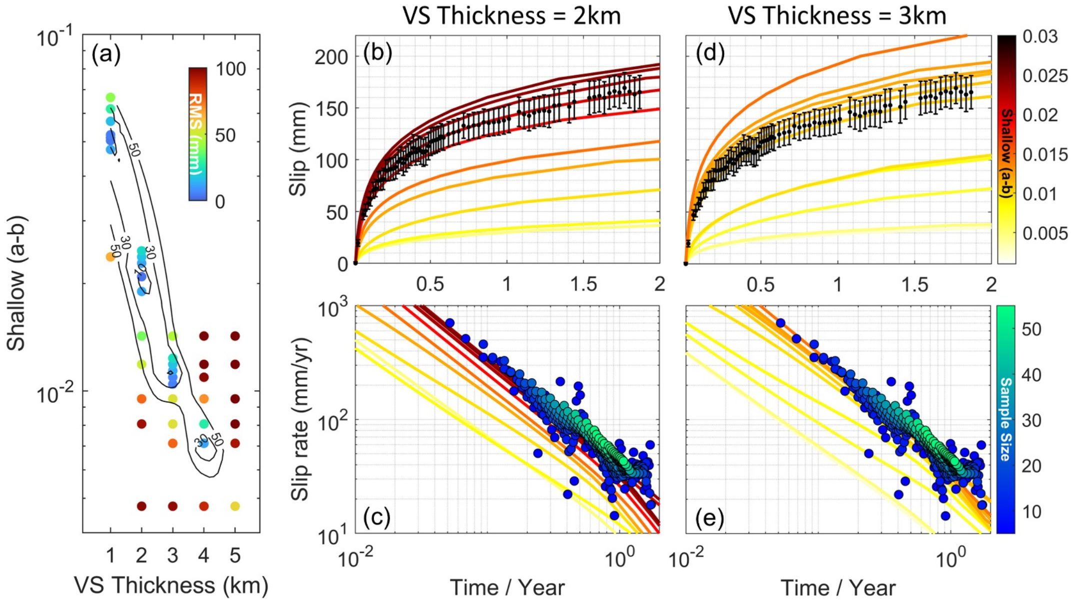

Figure 7. Analogous to Figure 6 but for postseismic deformation in Box 2 shown in Figure 2.

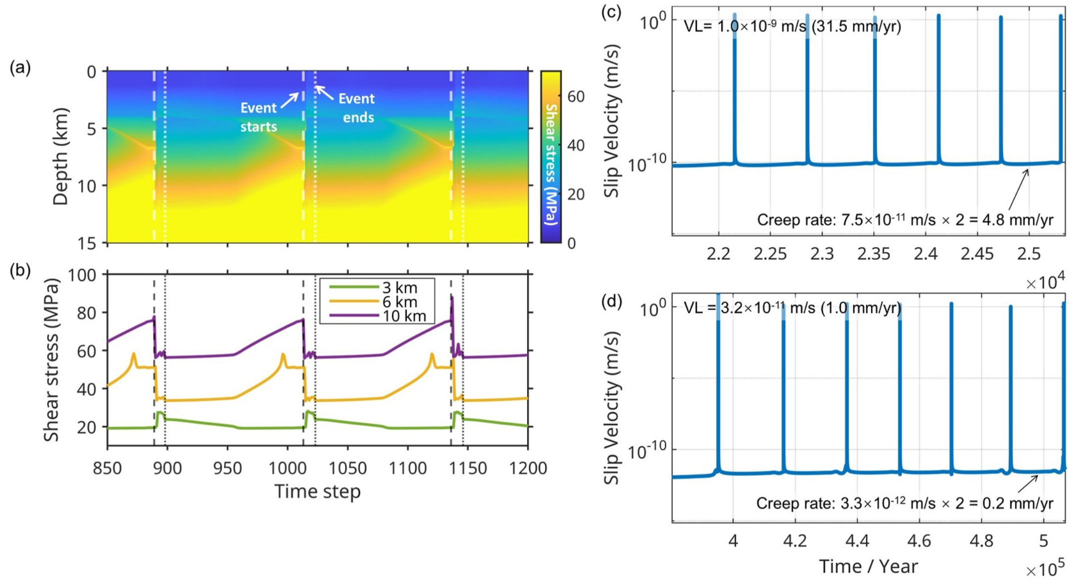

Figure 8. (a) Modeled shear stress as a function of model time step. The dash line respresents the time of an earthquake starts, defined as when the maximum slip velocity exceeds 1 mm/s. The dot line respresents the time of an earthquake ends. In this model $(a - b) = 0.0095$ and $T_{vs} = 4$ km. (b) Time series of the modeled shear stress in 3, 6, and 10 km in depth. (c) Modeled surface velocity for multiple earthquake cycles based on a loading rate of 31.5 mm/yr. The interseismic creep rate is calculated with the last cycle results. (d) Analogous to (c) but for a loading rate of 1.0 mm/yr.

Values of $(a - b)$ determined by different methods and data can be variable even for the same earthquake. Wang and Fialko (2018) use a rate-strengthening law (assuming $b = 0$) to explain the postseismic deformation of 2015 Mw 7.8 Gorkha earthquake and found that $a = 6.5 \times 10^{-2}$, an order of magnitude larger than $a = (0.8–1.6) \times 10^{-3}$ estimated by Ingleby et al. (2020). Our experiments show a strong dependency of frictional parameters on the thickness of the shallow rate-strengthening layer, which could offer a potential explanation to the discrepancy.

To understand how the slip rate evolves over time, we compare the modeled and observed postseismic slip rates. We calculate the postseismic surface velocity over different time intervals using a piecewise linear fitting technique (Ingleby & Wright, 2017). The data is fitted across sample windows ranging from 5 to 55 epochs, in increments of 5, with a step size of 1. A log-log plot reveals a linear-like decay of slip rate with time, consistent with the Omori-like decay pattern observed in postseismic slip rates of continental earthquakes by Ingleby and Wright (2017). Comparing the observed and modeled slip rate versus time in the log-log domain, we again show the trade-off between optimal shallow (a, b) and VS thicknesses.

During the simulated earthquake, shear stress drops abruptly in the velocity-weakening region upon nucleation. Simultaneously, we observe a significant shear stress increase (~10 MPa at 3.0 km depth for model $(a - b) = 0.0095$ and $T_{vs} = 4$ km) in the shallow velocity-strengthening layer (Figures 8a and 8b). This rapid dynamic stress propagation from the deeper velocity-weakening rupture provides the necessary stress overshoot to trigger seismic slip in the stable shallow velocity-strengthening region. Following the coseismic phase, this region continues to slip as postseismic creep, directly accounting for the observed overlap in our geodetic inversions.

Our dynamic model indicates that a shallow velocity-strengthening layer is a necessary condition to reproduce the observed overlap between coseismic and postseismic slip. This model also results in a significant amount of interseismic creep, which is directly proportional to tectonic loading rate. The interseismic creep rate is only 0.2 mm/yr, with a loading rate $V_l = 1.0$ mm/yr, while creep rate is 4.8 mm/yr with $V_l = 31.5$ mm/yr (Figures 8c and 8d). Other parameters also affect the value of interseismic creep rate but not as significant as V_l. Reducing T_{vs} slightly decreases the creep rate (4.8 vs. 3.0 mm/yr) (Figure 8c; Figure S34a in Supporting Information S1) while changing $(a - b)$ has little impact on the creep rate (4.8 vs. 5.1 mm/yr) (Figure 8c'; Figure S34b in Supporting Information S1).

We find that the dynamic afterslip model agrees well with the kinematic model at depths greater than ∼3 km, whereas noticeable discrepancies occur in the shallow portion. The physical parameters of the dynamic model are constrained using postseismic displacement at locations ∼2 km from the fault, where the observed deformation is likely dominated by somewhat deeper afterslip rather than near-surface slip. In addition. In addition, the assumption of a uniform shallow $(a - b)$ for each model and choice of patch size in kinematic model, may also contribute to the mismatch. Allowing heterogeneous frictional parameters along depth would likely provide a more realistic representation.

While an optimal combination of parameters (e.g., D_c, $a - b$, T_{vs}, V_l) could theoretically fit the coseismic, postseismic, and interseismic signals simultaneously, such an optimization is beyond the scope of this work due to high computational costs and the simplified geometry of our model. Instead, we focus on providing first-order constraints on shallow frictional parameters using postseismic time series to explore the mechanisms underlying overlapping slip behavior. Since interseismic creep is required by the optimal model, we further analyze the interseismic InSAR velocity to explore the potential creep along the Jiangcuo Fault, and discuss the possbile causes to the overlapping slip in the following section.

5. Discussion

5.1. Interseismic Creep Modeling

The interseismic creep rate derived from dynamic earthquake cycle models is 0.2 mm/yr, with a loading rate 1.0 mm/yr. The interseimsic creep rate would be smaller with a lower loading rate, such as the estimated geological slip rate of Jiangcuo Fault. The uncertainty in the InSAR V_E data in this region is as high as 1.0 mm/yr (Figure S10a in Supporting Information S1), which is equivalent to the geodetic slip rate (Jian et al., 2022; Zhu et al., 2021) and larger than geological slip rate (Pan et al., 2022). We use a simple velocity profile across the Jiangcuo Fault with a screw dislocation model to investigate the slip rate and potential creep rate:

$$V_{\text{para}}(x) = \frac{S}{\pi}\arctan\left(\frac{x}{d_1}\right) - C\left[\frac{1}{\pi}\arctan\left(\frac{x}{d_2}\right) - \mathcal{H}(x)\right] + D \quad (4)$$

where $V_{\text{para}}(x)$ is the fault-parallel velocity, x is the distance to the fault, S is the slip rate, d_1 is the locking depth, C is the creep rate, d_2 is the creep depth, $\mathcal{H}(x)$ is the Heaviside function, D is a static offset. We use both unfiltered and filtered data to conduct the inversion. Three additional faults were included in the model: the East Kunlun Fault, Dari Fault and Qingshuihe Fault. For these three faults we solve the slip rate and locking depth, leading to a total of 11 free parameters. The prior constraints of each parameter are shown in Table S3 of Supporting Information S1. The model runs 40,000 iterations and generates 60,000 samples of the posterior distribution. We estimate the maximum a posteriori probability (MAP) solutions and their uncertainties of each parameter for both unfiltered (Figure S35 in Supporting Information S1) and filtered (Figure S36 in Supporting Information S1) profiles.

The slip rate of the East Kunlun Fault inverted from filtered data is $8.0^{+0.1}_{-0.1}$ mm/yr (Figure 9a), giving rise to a strain rate of $s/\pi d = 93.3$ nst/yr based on the estimated $28.7^{+0.5}_{-0.5}$ km of locking depth. Slip rates of the East Kunlun Fault are well resolved using both filtered and unfiltered data. Although we observe velocity steps across the Jiangcuo Fault in the unfiltered data, the modeled creep rate is $0.6^{+0.1}_{-0.2}$ mm/yr, which is smaller than uncertainties of InSAR V_E in this region (Figure S10a in Supporting Information S1). The step across the Jiangcuo Fault is smoothed after applying the median filter, leading to a steady slope along the profile. We perform a series of 1-D synthetic test on profiles generated by screw dislocation model, with a slip rate of 1.0 or 0.5 mm/yr, creep rate of 0.5 mm/yr and Gaussian noise of 0.5 mm/yr (Figure S37 in Supporting Information S1). We apply a median filter on the data with different filter window sizes and invert the slip and creep rate with the same Bayesian approach. Synthetic tests suggest that slip gradient across a strike slip fault with Gaussian noise in the data can be well isolated by median filter and inversion process, despite the locking depth and creep depth being poorly resolved. Hence, the velocity step across these three faults may be caused by other non-Gaussian noise, such as topography-related tropospheric noise. Both the slip and creep rate of Jiangcuo Fault derived from the filtered profile data are less than 0.1 mm/yr, which is much lower than uncertainties of InSAR observations. Therefore, any interseismic creep of Jiangcuo Fault is very low, and less than predicted by the dynamic model.

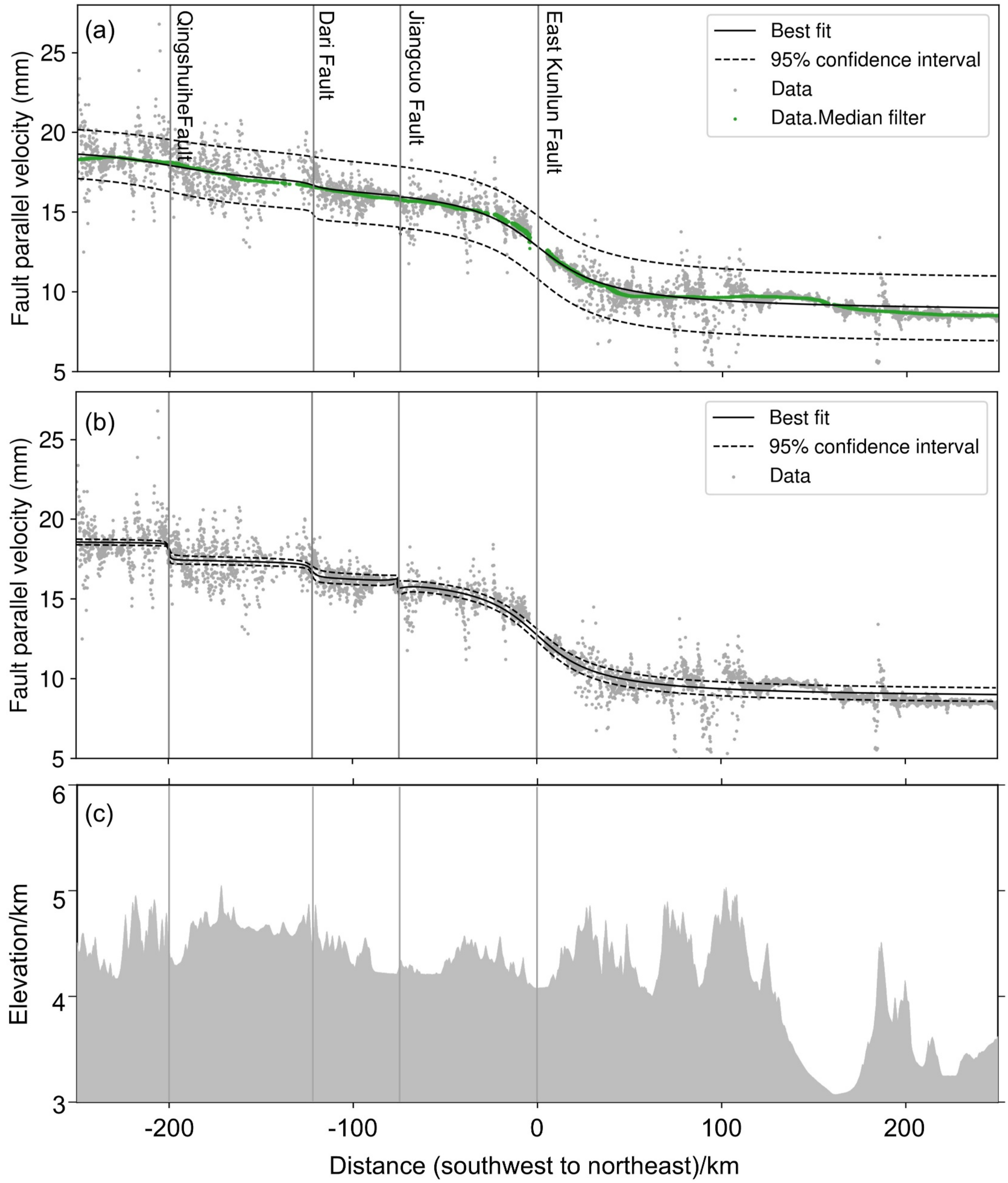

Figure 9. (a) Profile of data (gray dots) and data after median filter (green dots). Black solid line represents the best-fit dislocation model across multiple faults based on data after median filter. Black dash lines represent model within 95% confidence interval. (b) Analogous to (a) except that the model is based on data instead of data after median filter. (c) Profile of the topography.

5.2. Explanations for Overlap of Coseismic and Postseismic Slip

Our dynamic model successfully reproduced observed overlap of coseismic and aseismic slip in middle segment of the Jiangcuo Fault, despite the fact that no clear interseismic creep is captured by geodetic observations. Coexistence of interseismic and postseismic creep generated by the earthquake cycle model is supported by geodetic observations in other regions. For instance, GNSS observations indicate an interseismic creep rate of 1 ± 1 mm/yr on the western North Anatolian Fault at approximately 30.1°E (Hussain et al., 2016; Çakir et al., 2012). Field investigations of the 1999 Izmit earthquake recorded a coseismic offset exceeding 3 m at this location, with postseismic shallow slip of up to 0.3 m observed by InSAR and GNSS after 10 years (Hussain et al., 2016; Çakir et al., 2003). Similarly, interseismic creep on the Imperial Fault was first observed in the 1950s (Whitten, 1956),

10.1029/2025JB033035

with recent InSAR and GNSS data indicating a creep rate of 3.0–10.0 mm/yr (Lindsey & Fialko, 2016). Shallow coseismic and postseismic slip of the 1979 M 6.6 Imperial Valley earthquake was also recorded through trilateration and alignment surveys (Lindsey & Fialko, 2016). The lack of interseismic creep on the Jiangcuo Fault has two possible explanations: One is that the creep rate is as low as 0.2 mm/yr, as suggested by the numerical model, and below detection limit for InSAR. The other is that the fault is actually locked during interseismic period.

The presence of fluid injection following the main shock can elevate the pore pressure and reduce the effective normal stress, favoring aseismic slip. Transient elevation in pore pressure has been hypothesized to facilitate large afterslip in areas with negative coseismic Coulomb stress change in the 2010 Maule Mw 8.8 earthquake (Bedford et al., 2013), though this area is inferred to be locked during the interseismic period. Overlap of aseismic and seismic slip on the Chaman Fault has been explained by a velocity-weakening regime within complex fault geometry and fluid conditions (Dalaison et al., 2021). Elevated pore fluid pressure may provide a possible explanation for postseismic slip in coseismic slip areas of the Maduo earthquake. For a locked fault, postseismic slip is possible if the pore fluid pressure significantly increases and is maintained for a long time after the earthquake (Dianala et al., 2020), in which case we need mechanisms other than the shallow rate-strengthening layer to explain the overlap of coseismic and postseismic slip.

The Maduo earthquake triggered widespread seismic soil liquefaction along the Jiangcuo Fault, suggesting that this region is water-saturated and susceptible to fluid-related activity (Wang et al., 2023; Yuan et al., 2022). The lithology in sedimentary layer surrounding the Jiangcuo Fault consists primarily of sandstone (Figure S38 in Supporting Information S1) (Fang et al., 2022; Pan et al., 2022; Wang et al., 2023), a porous rock that can function as an aquifer, storing significant amounts of fluid (David et al., 1994; Kitamura et al., 2010). A dense seismic array was deployed across the middle segment (approximately location range: 98.4°E–98.6°E) of the Jiangcuo Fault to derive the crustal structure model after the earthquake (Guo et al., 2022; Wu et al., 2022). The distance between adjacent seismic stations was 0.5–1.0 km and the observation time was from 05 June 2022 to 03 July 2022 (Guo et al., 2022). The crustal structure model derived from P-wave travel times show low-velocity anomalies at approximately 4 km depth below the fault (Wu et al., 2022), suggesting the possible existence of fluid. Fluid will migrate upward along a porous fault zone when pressure gradients exceed the hydrostatic gradient, as the fault permeability is higher than the surrounding rocks (Rice, 1992; Zoback & Byerlee, 1975). During coseismic events, extensive cracking at the grain scale may open more path for fluid to upwell (David et al., 1994). Although sealing/healing processes after an earthquake may discharge fluid from the fault zone and decrease permeability, the exact time scale for this process is poorly constrained. Pressure solution crack-sealing modeling suggests time scales of this process could last a few days to thousands of years (Gratier et al., 2003). If low permeability of surrounding rock acts as a seal layer and sealing/healing time is long, fluid would be maintained in fault zone for a long time, leading to fluid overpressure and weakening effective normal stress, facilitating aseismic slip.

Another possible mechanism that can weaken the fault is coseismic shear heating which produces a thermal anomaly that changes the material property from velocity-weakening to velocity-strengthening. Thomas et al. (2017) suggested that coseismic shear heating may provide an explanation for the afterslip that occurred at deep layer of rupture area in middle section of fault of the 2003 Mw 6.8 Chenkung earthquake. Laboratory experiment shows that such transition starts at a temperature of roughly 300°C, which is about at the depth of 11–13 km in the continental crust (Aharonov & Scholz, 2019; Blanpied et al., 1991), while other experiments show unstable slip can occur at temperatures as high as 600°C (Mitchell et al., 2016). Numerical simulations suggest that significant temperature changes due to coseismic shear heating typically occur below depths of 8.0 km (Thomas et al., 2017). However, overlap of coseismic and postseismic slip occurs in fault's shallow part and hence unlikely due to shear heating.

5.3. Implication for Shallow Slip Deficit

Coseismic slip distributions derived from InSAR observation of strike slip earthquakes indicate that slip decays from middle of the depth range to the shallow part (Fialko et al., 2005; Hussain et al., 2018). Possible explanations for the shallow slip deficit includes poorly-constrained near field observations, homogeneous elastic medium during inversion, off-fault inelastic deformation and aseismic slip on the shallow faults (Fialko et al., 2005; Marchandon et al., 2021). Clear shallow slip deficit of the Maduo earthquake was observed from published coseismic slip models (Fang et al., 2022, and references therein), partially due to lack of near fault InSAR

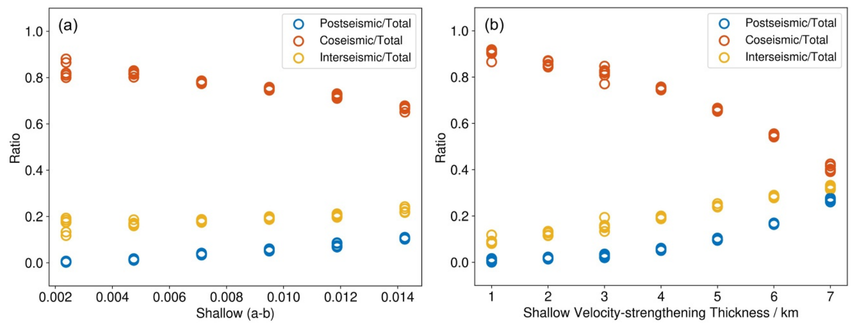

Figure 10. (a) Modeled ratio of cumulative interseismic, coseismic and postseismic to total slip, with different value of $(a-b)$ and fixed $T_{vs}=4.0$ km. Results of six earthquake cycle are plotted for each simulation. (b) Analogous to (a) but with different value of T_{vs} and fixed $(a-b)=0.0095$.

observations (Marchandon et al., 2021) arising from unwrapping errors caused by larger slip gradient. Jin et al. (2023) noted that 1 year of shallow afterslip of Maduo earthquake accounts for less than 5% of the coseismic deficit. Postseismic slip of the 1999 Izmit earthquake after projecting the afterslip model 200 years forwards accounted for 30%–65% of shallow slip deficit (Hussain et al., 2018). Here we investigate the contribution from interseismic shallow creep to shallow slip defict.

Using the dynamic model, we investigated the proportion of slip in the shallow velocity-strengthening layer occurring at different phases over time (Figure 10). Though the slip deficit is fully compensated after one earthquake cycle, it allows us to understand how the slip partitions during different earthquake stages and what the controls on this are. Increasing the value of $(a-b)$ and/or the shallow velocity-strengthening thickness increases the proportion of interseismic and postseismic slip. Interseismic creep accounts for ~20% of total slip for models with $T_{vs}=4.0$ km and variable $(a-b)$. In all scenarios cumulative interseismic slip is larger than the postseismic slip. For faults with very low creep rate, such as 0.2 mm/yr in our model, the integrated interseismic creep can reach to 1.3 m, with a recurrence interval of 6500 years of Jiangcuo Fault (Pan et al., 2022). Therefore, for a low slip rate fault with long earthquake recurrence interval, a very low creep would make a significant contribution to diminishing the shallow slip deficit over an entire earthquake cycle.

6. Conclusions

We use InSAR observations before and after the 2021 Maduo Mw 7.4 earthquake, incorporating kinematic inversion and dynamic earthquake cycle simulation, to investigate the mechanism for overlap between shallow coseismic and postseismic slips. We find that:

1. Kinematic models show that significant shallow afterslip occurred on the fault's centeral segment, where large coseismic slip also happened.
2. Dynamics models including a shallow velocity-strengthening layer are capable of generating coseismic rupture and postseismic afterslip in the same shallow layer. Such models also predict interseismic creep.
3. No clear creep has been found across the Jiangcuo Fault. The creep rate from the earthquake cycle model is no more than 0.2 mm/yr, given the loading rate of 1.0 mm/yr. Creep on the Jiangcuo Fault maybe below the detection threshold for InSAR observations. Alternatively, fluid upwelling during coseismic period may lower the effective normal stress and promote afterslip.
4. For a shallow velocity-strengthening layer on a slow slip fault with long earthquake recurrence interval, a very low creep would still make a significant contribution to diminishing the shallow slip deficit over an entire earthquake cycle.

Conflict of Interest

The authors declare no conflicts of interest relevant to this study.

Availability Statement

The interferograms used in this study can be freely downloadable from https://comet.nerc.ac.uk/comet-lics-portal/. The slip inversion code is available from Amey et al. (2018). The earthquake cycle modelling code is available from Allison and Dunham (2018). The horizontal GNSS velocity used in this study is from Wang and Shen (2020) and is downloadable from Shen (2019). The vertical GNSS velocity is from Zhao et al. (2023) and is downloadable from Zhao et al. (2022). The decomposed InSAR velocity, postseismic InSAR time series, geodetic slip models, earthquake cycle models in this work are available at Gao et al. (2025).

Acknowledgments

Yuan Gao is supported by the China Scholarship Council (CSC) as a visiting PhD student at the University of Leeds (202106567012). COMET is the UK Natural Environment Research Council (NERC)'s Centre for the Observation and Modelling of Earthquakes, Volcanoes and Tectonics, a partnership between UK Universities and the British Geological Survey. Slip inversion and earthquake cycle modelling were undertaken on ARC4, part of the High Performance Computing facilities at the University of Leeds. LiCSAR contains modified Copernicus Sentinel data analyzed by COMET. LiCSAR uses JASMIN, the UK's collaborative data analysis environment (http://jasmin.ac.uk/).This work is also supported by the National Natural Science Foundation of China (42174006, 42090055), Science Fund for Distinguished Young Scholars of Shaanxi Province (2022JC-18), and Fundamental Research Funds for the Central Universities (2025-KJJC-A03, 2025QN1105). Figures were produced using the Generic Mapping Tools (Wessel et al., 2019), Python and Matlab. We thank the editor and reviewers for their thoughtful comments which greatly improved the manuscript.

References

Aharonov, E., & Scholz, C. H. (2019). The brittle-ductile transition predicted by a physics-based friction law. *Journal of Geophysical Research: Solid Earth*, *124*(3), 2721–2737. https://doi.org/10.1029/2018JB016878

Allison, K. L., & Dunham, E. M. (2018). Earthquake cycle simulations with rate-and-state friction and power-law viscoelasticity. *Tectonophysics*, *733*, 232–256. https://doi.org/10.1016/j.tecto.2017.10.021

Allison, K. L., & Dunham, E. M. (2021). Influence of shear heating and thermomechanical coupling on earthquake sequences and the brittle-ductile transition. *Journal of Geophysical Research: Solid Earth*, *126*(6), e2020JB021394. https://doi.org/10.1029/2020JB021394

Amey, R. M. J., Hooper, A., & Walters, R. J. (2018). A bayesian method for incorporating self-similarity into earthquake slip inversions. *Journal of Geophysical Research: Solid Earth*, *123*(7), 6052–6071. https://doi.org/10.1029/2017JB015316

Ansari, H., De Zan, F., & Parizzi, A. (2021). Study of systematic bias in measuring surface deformation with sar interferometry. *IEEE Transactions on Geoscience and Remote Sensing*, *59*(2), 1285–1301. https://doi.org/10.1109/TGRS.2020.3003421

Bagnardi, M., & Hooper, A. (2018). Inversion of surface deformation data for rapid estimates of source parameters and uncertainties: A bayesian approach. *Geochemistry, Geophysics, Geosystems*, *19*(7), 2194–2211. https://doi.org/10.1029/2018GC007585

Barbot, S., Fialko, Y., & Bock, Y. (2009). Postseismic deformation due to the mw 6.0 2004 parkfield earthquake: Stress-driven creep on a fault with spatially variable rate-and-state friction parameters. *Journal of Geophysical Research*, *114*(B7). https://doi.org/10.1029/2008JB005748

Barker, T. G. (1976). Quasi-static motions near the San Andreas Fault Zone. *Geophysical Journal International*, *45*(3), 689–705. https://doi.org/10.1111/j.1365-246X.1976.tb06918.x

Barnhart, W. D., Murray, J. R., Briggs, R. W., Gomez, F., Miles, C. P. J., Svarc, J., et al. (2016). Coseismic slip and early afterslip of the 2015 illapel, Chile, earthquake: Implications for frictional heterogeneity and coastal uplift. *Journal of Geophysical Research: Solid Earth*, *121*(8), 6172–6191. https://doi.org/10.1002/2016JB013124

Bedford, J., Moreno, M., Baez, J. C., Lange, D., Tilmann, F., Rosenau, M., et al. (2013). A high-resolution, time-variable afterslip model for the 2010 maule mw = 8.8, Chile megathrust earthquake. *Earth and Planetary Science Letters*, *383*, 26–36. https://doi.org/10.1016/j.epsl.2013.09.020

Blanpied, M. L., Lockner, D. A., & Byerlee, J. D. (1991). Fault stability inferred from granite sliding experiments at hydrothermal conditions. *Geophysical Research Letters*, *18*(4), 609–612. https://doi.org/10.1029/91GL00469

Blanpied, M. L., Lockner, D. A., & Byerlee, J. D. (1995). Frictional slip of granite at hydrothermal conditions. *Journal of Geophysical Research*, *100*(B7), 13045–13064. https://doi.org/10.1029/95JB00862

Çakir, Z., Chabalier, J.-B. d., Armijo, R., Meyer, B., Barka, A., & Peltzer, G. (2003). Coseismic and early post-seismic slip associated with the 1999 izmit earthquake (Turkey), from sar interferometry and tectonic field observations. *Geophysical Journal International*, *155*(1), 93–110. https://doi.org/10.1046/j.1365-246x.2003.02001.x

Çakir, Z., Ergintav, S., Özener, H., Dogan, U., Akoglu, A. M., Meghraoui, M., & Reilinger, R. (2012). Onset of aseismic creep on major strike-slip faults. *Geology*, *40*(12), 1115–1118. https://doi.org/10.1130/g33522.1

Chen, C., & Zebker, H. (2002). Phase unwrapping for large sar interferograms: Statistical segmentation and generalized network models. *IEEE Transactions on Geoscience and Remote Sensing*, *40*(8), 1709–1719. https://doi.org/10.1109/TGRS.2002.802453

Chen, F., Diao, F., Haghighi, M. H., Wang, Y., Zhu, Y., Wang, R., & Xiong, X. (2024). Mechanism and implications of the post-seismic deformation following the 2021 Mw 7.4 Maduo (Tibet) earthquake. *Geophysical Journal International*, *237*(1), 203–216. https://doi.org/10.1093/gji/ggae034

Chen, K., Avouac, J.-P., Geng, J., Liang, C., Zhang, Z., Li, Z., & Zhang, S. (2022). The 2021 mw 7.4 madoi earthquake: An archetype bilateral slip-pulse rupture arrested at a splay fault. *Geophysical Research Letters*, *49*(2), e2021GL095243. https://doi.org/10.1029/2021gl095243

Dalaison, M., Jolivet, R., van Rijsingen, E. M., & Michel, S. (2021). The interplay between seismic and aseismic slip along the chaman fault illuminated by insar. *Journal of Geophysical Research: Solid Earth*, *126*(12), e2021JB021935. https://doi.org/10.1029/2021JB021935

Daout, S., Dini, B., Haeberli, W., Doin, M.-P., & Parsons, B. (2020). Ice loss in the northeastern Tibetan Plateau permafrost as seen by 16 yr of esa sar missions. *Earth and Planetary Science Letters*, *545*, 116404. https://doi.org/10.1016/j.epsl.2020.116404

David, C., Wong, T.-f., Zhu, W., & Zhang, J. (1994). Laboratory measurement of compaction-induced permeability change in porous rocks: Implications for the generation and maintenance of pore pressure excess in the crust. *Pure and Applied Geophysics*, *143*(1–3), 425–456. https://doi.org/10.1007/bf00874337

Dianala, J. D. B., Jolivet, R., Thomas, M. Y., Fukushima, Y., Parsons, B., & Walker, R. (2020). The relationship between seismic and aseismic slip on the Philippine fault on leyte island: Bayesian modeling of fault slip and geothermal subsidence. *Journal of Geophysical Research: Solid Earth*, *125*(12), e2020JB020052. https://doi.org/10.1029/2020JB020052

Dieterich, J. H. (1978). Time-dependent friction and the mechanics of stick-slip. *Pure and Applied Geophysics*, *116*, 790–806.

Dieterich, J. H., & Kilgore, B. D. (1994). Direct observation of frictional contacts: New insights for state-dependent properties. *Pure and Applied Geophysics*, *143*(1–3), 283–302. https://doi.org/10.1007/bf00874332

Erickson, B. A., Jiang, J., Barall, M., Lapusta, N., Dunham, E. M., Harris, R., et al. (2020). The community code verification exercise for simulating sequences of earthquakes and aseismic slip (SEAS). *Seismological Research Letters*, *91*(2A), 874–890. https://doi.org/10.1785/0220190248

Fang, J., Ou, Q., Wright, T. J., Okuwaki, R., Amey, R. M. J., Craig, T. J., et al. (2022). Earthquake cycle deformation associated with the 2021 mw 7.4 maduo (eastern Tibet) earthquake: An intrablock rupture event on a slow-slipping fault from sentinel-1 insar and teleseismic data. *Journal of Geophysical Research: Solid Earth*, *127*(11), e2022JB024268. https://doi.org/10.1029/2022JB024268

Fialko, Y., Sandwell, D., Simons, M., & Rosen, P. (2005). Three-dimensional deformation caused by the bam, Iran, earthquake and the origin of shallow slip deficit. *Nature*, *435*(7040), 295–299. https://doi.org/10.1038/nature03425
Gao, Y., Ou, Q., Fang, J., Carpenter, M., Wright, T., Allison, K., et al. (2025). Geodetic constraints on fault kinematics and dynamics of 2021 maduo earthquake: Implications for fault friction (version 0.0) [Dataset]. *Zenodo*. https://doi.org/10.5281/zenodo.17181812
Goodman, J., & Weare, J. (2010). Ensemble samplers with affine invariance. *Communications in Applied Mathematics and Computational Science*, *5*(1), 65–80. https://doi.org/10.2140/camcos.2010.5.65
Gratier, J.-P., Favreau, P., & Renard, F. (2003). Modeling fluid transfer along California faults when integrating pressure solution crack sealing and compaction processes. *Journal of Geophysical Research*, *108*(B2). https://doi.org/10.1029/2001JB000380
Guo, H., Chang, L., Lu, L., Wu, P., Lü, M., & Ding, Z. (2022). High-resolution earthquake catalog for the focal area of the Qinghai madoi m s 7.4 earthquake based on deep-learning phase picker and dense array. *Chinese Journal of Geophysics*, *65*(5), 1628–1643.
Hussain, E., Wright, T. J., Walters, R. J., Bekaert, D., Hooper, A., & Houseman, G. A. (2016). Geodetic observations of postseismic creep in the decade after the 1999 izmit earthquake, Turkey: Implications for a shallow slip deficit. *Journal of Geophysical Research: Solid Earth*, *121*(4), 2980–3001. https://doi.org/10.1002/2015JB012737
Hussain, E., Wright, T. J., Walters, R. J., Bekaert, D. P., Lloyd, R., & Hooper, A. (2018). Constant strain accumulation rate between major earthquakes on the north anatolian fault. *Nature Communications*, *9*(1), 1392. https://doi.org/10.1038/s41467-018-03739-2
Ingleby, T., & Wright, T. J. (2017). Omori-like decay of postseismic velocities following continental earthquakes. *Geophysical Research Letters*, *44*(7), 3119–3130. https://doi.org/10.1002/2017GL072865
Ingleby, T., Wright, T. J., Hooper, A., Craig, T. J., & Elliott, J. R. (2020). Constraints on the geometry and frictional properties of the main himalayan thrust using coseismic, postseismic, and interseismic deformation in Nepal. *Journal of Geophysical Research: Solid Earth*, *125*(2), e2019JB019201. https://doi.org/10.1029/2019JB019201
Jian, H., Gong, W., Li, Y., & Wang, L. (2022). Bayesian inference of fault slip and coupling along the tuosuo lake segment of the kunlun fault, China. *Geophysical Research Letters*, *49*(7), e2021GL096882. https://doi.org/10.1029/2021gl096882
Jiang, J., Erickson, B. A., Lambert, V. R., Ampuero, J.-P., Ando, R., Barbot, S. D., et al. (2022). Community-driven code comparisons for three-dimensional dynamic modeling of sequences of earthquakes and aseismic slip. *Journal of Geophysical Research: Solid Earth*, *127*(3), e2021JB023519. https://doi.org/10.1029/2021JB023519
Jin, Z., Fialko, Y., Yang, H., & Li, Y. (2023). Transient deformation excited by the 2021 m7.4 maduo (China) earthquake: Evidence of a deep shear zone. *Journal of Geophysical Research: Solid Earth*, *128*(8), e2023JB026643. https://doi.org/10.1029/2023JB026643
Jin, Z., Fialko, Y., Zubovich, A., & Schöne, T. (2022). Lithospheric deformation due to the 2015 m7.2 sarez (pamir) earthquake constrained by 5 years of space geodetic observations. *Journal of Geophysical Research: Solid Earth*, *127*(4), e2021JB022461. https://doi.org/10.1029/2021JB022461
Johnson, K. M., Fukuda, J., & Segall, P. (2012). Challenging the rate-state asperity model: Afterslip following the 2011 m9 tohoku-oki, Japan, earthquake. *Geophysical Research Letters*, *39*(20). https://doi.org/10.1029/2012GL052901
Kaneko, Y., & Fialko, Y. (2011). Shallow slip deficit due to large strike-slip earthquakes in dynamic rupture simulations with elasto-plastic off-fault response. *Geophysical Journal International*, *186*(3), 1389–1403. https://doi.org/10.1111/j.1365-246X.2011.05117.x
Kaneko, Y., Fialko, Y., Sandwell, D. T., Tong, X., & Furuya, M. (2013). Interseismic deformation and creep along the central section of the north anatolian fault (Turkey): Insar observations and implications for rate-and-state friction properties. *Journal of Geophysical Research: Solid Earth*, *118*(1), 316–331. https://doi.org/10.1029/2012JB009661
Kitamura, K., Takahashi, M., Mizoguchi, K., Masuda, K., Ito, H., & Song, S.-R. (2010). Effects of pressure on pore characteristics and permeability of porous rocks as estimated from seismic wave velocities in cores from tcdp hole-a. *Geophysical Journal International*, *182*(3), 1148–1160. https://doi.org/10.1111/j.1365-246x.2010.04694.x
Lachenbruch, A. H., & Sass, J. H. (1980). Heat flow and energetics of the san andreas fault zone. *Journal of Geophysical Research*, *85*(B11), 6185–6222. https://doi.org/10.1029/JB085iB11p06185
Lapusta, N., & Rice, J. R. (2003). Nucleation and early seismic propagation of small and large events in a crustal earthquake model. *Journal of Geophysical Research*, *108*, B4. https://doi.org/10.1029/2001JB000793
Lapusta, N., Rice, J. R., Ben-Zion, Y., & Zheng, G. (2000). Elastodynamic analysis for slow tectonic loading with spontaneous rupture episodes on faults with rate- and state-dependent friction. *Journal of Geophysical Research*, *105*(B10), 23765–23789. https://doi.org/10.1029/2000JB900250
Lazecký, M., Fang, J., Hooper, A., & Wright, T. (2022). Improved phase unwrapping algorithm based on standard methods. In *Igarss 2022 - 2022 ieee international geoscience and remote sensing symposium* (pp. 743–746). https://doi.org/10.1109/IGARSS46834.2022.9884337
Lazecký, M., Spaans, K., González, P. J., Maghsoudi, Y., Morishita, Y., Albino, F., et al. (2020). Licsar: An automatic insar tool for measuring and monitoring tectonic and volcanic activity. *Remote Sensing*, *12*(15), 2430. https://doi.org/10.3390/rs12152430
Lemrabet, L., Doin, M.-P., Lasserre, C., & Durand, P. (2023). Referencing of continental-scale insar-derived velocity fields: Case study of the eastern Tibetan Plateau. *Journal of Geophysical Research: Solid Earth*, *128*(7), e2022JB026251. https://doi.org/10.1029/2022JB026251
Li, Z., Xiong, W., Hooper, A., Zhao, Z., Gao, Y., Elliott, J. R., et al. (2025). Imaging viscosity after the 2021 mw 7.4 maduo earthquake: Insights on the regional rheology variation beneath the bayan har block. *Earth and Planetary Science Letters*, *666*, 119465. https://doi.org/10.1016/j.epsl.2025.119465
Liang, S., Gan, W., Shen, C., Xiao, G., Liu, J., Chen, W., et al. (2013). Three-dimensional velocity field of present-day crustal motion of the Tibetan Plateau derived from gps measurements. *Journal of Geophysical Research: Solid Earth*, *118*(10), 5722–5732. https://doi.org/10.1002/2013JB010503
Lindsey, E. O., & Fialko, Y. (2016). Geodetic constraints on frictional properties and earthquake hazard in the imperial valley, southern California. *Journal of Geophysical Research: Solid Earth*, *121*(2), 1097–1113. https://doi.org/10.1002/2015JB012516
Liu, Y.-K., Yunjun, Z., & Simons, M. (2025). Inferring tectonic plate rotations from insar time series. *Geophysical Research Letters*, *52*(12), e2025GL115137. https://doi.org/10.1029/2025gl115137
Lohman, R. B., & Simons, M. (2005). Some thoughts on the use of insar data to constrain models of surface deformation: Noise structure and data downsampling. *Geochemistry, Geophysics, Geosystems*, *6*(1), Q01007. https://doi.org/10.1029/2004GC000841
Marchandon, M., Hollingsworth, J., & Radiguet, M. (2021). Origin of the shallow slip deficit on a strike slip fault: Influence of elastic structure, topography, data coverage, and noise. *Earth and Planetary Science Letters*, *554*, 116696. https://doi.org/10.1016/j.epsl.2020.116696
Marone, C. (1998). Laboratory-derived friction laws and their application to seismic faulting. *Annual Review of Earth and Planetary Sciences*, *26*(1), 643–696. https://doi.org/10.1146/annurev.earth.26.1.643
Marone, C., & Kilgore, B. (1993). Scaling of the critical slip distance for seismic faulting with shear strain in fault zones. *Nature*, *362*(6421), 618–621. https://doi.org/10.1038/362618a0

Marone, C. J., Scholtz, C. H., & Bilham, R. (1991). On the mechanics of earthquake afterslip. *Journal of Geophysical Research*, *96*(B5), 8441–8452. https://doi.org/10.1029/91JB00275

Meade, B. J. (2024). Kinematic afterslip patterns. *Geophysical Research Letters*, *51*(1), e2023GL105797. https://doi.org/10.1029/2023GL105797

Mitchell, E. K., Fialko, Y., & Brown, K. M. (2016). Velocity-weakening behavior of westerly granite at temperature up to 600°c. *Journal of Geophysical Research: Solid Earth*, *121*(9), 6932–6946. https://doi.org/10.1002/2016JB013081

Molina-Ormazabal, D., Ampuero, J.-P., & Tassara, A. (2023). Diverse slip behaviour of velocity-weakening fault barriers. *Nature Geoscience*, *16*(12), 1200–1207. https://doi.org/10.1038/s41561-023-01312-1

Morishita, Y., Lazecky, M., Wright, T. J., Weiss, J. R., Elliott, J. R., & Hooper, A. (2020). Licsbas: An open-source insar time series analysis package integrated with the licsar automated sentinel-1 insar processor. *Remote Sensing*, *12*(3), 424. https://doi.org/10.3390/rs12030424

Noda, H., & Lapusta, N. (2013). Stable creeping fault segments can become destructive as a result of dynamic weakening. *Nature*, *493*(7433), 518–521. https://doi.org/10.1038/nature11703

Ou, Q., Daout, S., Weiss, J. R., Shen, L., Lazecký, M., Wright, T. J., & Parsons, B. E. (2022). Large-scale interseismic strain mapping of the ne Tibetan Plateau from sentinel-1 interferometry. *Journal of Geophysical Research: Solid Earth*, *127*(6), e2022JB024176. https://doi.org/10.1029/2022JB024176

Pan, J., Li, H., Chevalier, M.-L., Tapponnier, P., Bai, M., Li, C., et al. (2022). Co-seismic rupture of the 2021, mw7.4 maduo earthquake (northern Tibet): Short-cutting of the kunlun fault big bend. *Earth and Planetary Science Letters*, *594*, 117703. https://doi.org/10.1016/j.epsl.2022.117703

Qiu, Q., Feng, L., Hermawan, I., & Hill, E. M. (2019). Coseismic and postseismic slip of the 2005 mw 8.6 nias-simeulue earthquake: Spatial overlap and localized viscoelastic flow. *Journal of Geophysical Research: Solid Earth*, *124*(7), 7445–7460. https://doi.org/10.1029/2018JB017263

Rice, J. R. (1992). Fault stress states, pore pressure distributions, and the weakness of the san andreas fault. In *International geophysics* (Vol. 51, pp. 475–503). Elsevier. https://doi.org/10.1016/s0074-6142(08)62835-1

Rice, J. R., Lapusta, N., & Ranjith, K. (2001). Rate and state dependent friction and the stability of sliding between elastically deformable solids. *Journal of the Mechanics and Physics of Solids*, *49*(9), 1865–1898. https://doi.org/10.1016/S0022-5096(01)00042-4

Rubey, W. W., & King Hubbert, M. (1959). Role of fluid pressure in mechanics of overthrust faulting: Ii. overthrust belt in geosynclinal area of western wyoming in light of fluid-pressure hypothesis. *Geological Society of America Bulletin*, *70*(2), 167–206.

Ruina, A. (1983). Slip instability and state variable friction laws. *Journal of Geophysical Research*, *88*(B12), 10359–10370. https://doi.org/10.1029/JB088iB12p10359

Savage, J. C. (1990). Equivalent strike-slip earthquake cycles in half-space and lithosphere-asthenosphere earth models. *Journal of Geophysical Research*, *95*(B4), 4873–4879. https://doi.org/10.1029/JB095iB04p04873

Scholz, C. (1988). The critical slip distance for seismic faulting. *Nature*, *336*(6201), 761–763. https://doi.org/10.1038/336761a0

Scholz, C. H. (1998). Earthquakes and friction laws. *Nature*, *391*(6662), 37–42. https://doi.org/10.1038/34097

Shen, L., Hooper, A., Elliott, J. R., & Wright, T. J. (2024). Variability in interseismic strain accumulation rate and style along the altyn tagh fault. *Nature Communications*, *15*(1), 6876. https://doi.org/10.1038/s41467-024-51116-z

Shen, Z. (2019). Present-day crustal deformation of continental China derived from gps and its tectonic implications [Dataset]. *Harvard Dataverse*. https://doi.org/10.7910/DVN/C1WE3N

Smith, W. H. F., & Wessel, P. (1990). Gridding with continuous curvature splines in tension. *Geophysics*, *55*(3), 293–305. https://doi.org/10.1190/1.1442837

Stephenson, O. L., Liu, Y.-K., Yunjun, Z., Simons, M., Rosen, P., & Xu, X. (2022). The impact of plate motions on long-wavelength insar-derived velocity fields. *Geophysical Research Letters*, *49*(21), e2022GL099835. https://doi.org/10.1029/2022GL099835

Tanikawa, W., & Shimamoto, T. (2009). Frictional and transport properties of the chelungpu fault from shallow borehole data and their correlation with seismic behavior during the 1999 chi-chi earthquake. *Journal of Geophysical Research*, *114*(B1). https://doi.org/10.1029/2008JB005750

Thomas, M. Y., Avouac, J.-P., & Lapusta, N. (2017). Rate-and-state friction properties of the longitudinal valley fault from kinematic and dynamic modeling of seismic and aseismic slip. *Journal of Geophysical Research: Solid Earth*, *122*(4), 3115–3137. https://doi.org/10.1002/2016JB013615

Wang, K., & Bürgmann, R. (2020). Probing fault frictional properties during afterslip updip and downdip of the 2017 mw 7.3 sarpol-e zahab earthquake with space geodesy. *Journal of Geophysical Research: Solid Earth*, *125*(11), e2020JB020319. https://doi.org/10.1029/2020JB020319

Wang, K., & Fialko, Y. (2018). Observations and modeling of coseismic and postseismic deformation due to the 2015 m 7.8 gorkha (nepal) earthquake. *Journal of Geophysical Research: Solid Earth*, *123*(1), 761–779. https://doi.org/10.1002/2017JB014620

Wang, K., Xu, X., & Hu, Y. (2024). 09). Kinematics of the 2023 kahramanmaraş earthquake doublet: Biased near-fault data and shallow slip deficit. *Seismological Research Letters*, *96*(2A), 828–837. https://doi.org/10.1785/0220240062

Wang, M., & Shen, Z.-K. (2020). Present-day crustal deformation of continental China derived from gps and its tectonic implications. *Journal of Geophysical Research: Solid Earth*, *125*(2), e2019JB018774. https://doi.org/10.1029/2019JB018774

Wang, W., Fang, L., Wu, J., Tu, H., Chen, L., Lai, G., & Zhang, L. (2021). Aftershock sequence relocation of the 2021 ms 7.4 maduo earthquake, Qinghai, China. *Science China Earth Sciences*, *64*(8), 1371–1380. https://doi.org/10.1007/s11430-021-9803-3

Wang, W., Liu-Zeng, J., Shao, Y., Wang, Z., Han, L., Shen, X., et al. (2023). Mapping of soil liquefaction associated with the 2021 mw 7.4 maduo (madoi) earthquake based on the uav photogrammetry technology. *Remote Sensing*, *15*(4), 1032. https://doi.org/10.3390/rs15041032

Wei, M., Kaneko, Y., Liu, Y., & McGuire, J. J. (2013). Episodic fault creep events in California controlled by shallow frictional heterogeneity. *Nature Geoscience*, *6*(7), 566–570. https://doi.org/10.1038/ngeo1835

Weiss, J. R., Walters, R. J., Morishita, Y., Wright, T. J., Lazecky, M., Wang, H., et al. (2020). High-resolution surface velocities and strain for Anatolia from sentinel-1 insar and gnss data. *Geophysical Research Letters*, *47*(17), e2020GL087376. https://doi.org/10.1029/2020GL087376

Wessel, P., Luis, J. F., Uieda, L. a., Scharroo, R., Wobbe, F., Smith, W. H., & Tian, D. (2019). The generic mapping tools version 6. *Geochemistry, Geophysics, Geosystems*, *20*(11), 5556–5564. https://doi.org/10.1029/2019gc008515

Whitten, C. A. (1956). Crustal movement in California and Nevada. *EOS Transactions of the American Geophysical Union*, *37*(4), 393–398.

Wright, T. J., Parsons, B. E., & Lu, Z. (2004). Toward mapping surface deformation in three dimensions using insar. *Geophysical Research Letters*, *31*(1), L01607. https://doi.org/10.1029/2003GL018827

Wu, P., Chang, L., Lu, L., Guo, H., Lv, M., & Ding, Z. (2022). Three-dimensional fine velocity structure of the upper crust of the 2021 madoi m s 7.4 earthquake, Qinghai. *Chinese Journal of Geophysics*, *65*(6), 2006–2021.

Xu, L., Yunjun, Z., Ji, C., Meng, L., Fielding, E. J., Zinke, R., & Bao, H. (2023). Understanding the rupture kinematics and slip model of the 2021 mw 7.4 maduo earthquake: A bilateral event on bifurcating faults. *Journal of Geophysical Research: Solid Earth*, *128*(4), e2022JB025936. https://doi.org/10.1029/2022jb025936

Yu, C., Li, Z., Penna, N. T., & Crippa, P. (2018). Generic atmospheric correction model for interferometric synthetic aperture radar observations. *Journal of Geophysical Research: Solid Earth*, *123*(10), 9202–9222. https://doi.org/10.1029/2017JB015305

Yuan, J., Wang, Y., Zhan, B., Yuan, X., Wu, X., & Ma, J. (2022). Comprehensive investigation and analysis of liquefaction damage caused by the ms7.4 maduo earthquake in 2021 on the Tibetan Plateau, China. *Soil Dynamics and Earthquake Engineering*, *155*, 107191. https://doi.org/10.1016/j.soildyn.2022.107191

Zhao, Q., Chen, Q., van Dam, T., She, Y., & Wu, W. (2023). The vertical velocity field of the Tibetan Plateau and its surrounding areas derived from gps and surface mass loading models. *Earth and Planetary Science Letters*, *609*, 118107. https://doi.org/10.1016/j.epsl.2023.118107

Zhao, Q., Chen, Q., van Dam, T., Yawen, S., & Weiwei, W. (2022). The vertical velocity field of the Tibetan Plateau and its surrounding areas derived from gps and surface mass loading models [Dataset]. *Zenodo*. https://doi.org/10.5281/zenodo.5541386

Zheng, G., Wang, H., Wright, T. J., Lou, Y., Zhang, R., Zhang, W., et al. (2017). Crustal deformation in the india-eurasia collision zone from 25 years of gps measurements. *Journal of Geophysical Research: Solid Earth*, *122*(11), 9290–9312. https://doi.org/10.1002/2017JB014465

Zhu, W., Allison, K. L., Dunham, E. M., & Yang, Y. (2020). Fault valving and pore pressure evolution in simulations of earthquake sequences and aseismic slip. *Nature Communications*, *11*(1), 4833. https://doi.org/10.1038/s41467-020-18598-z

Zhu, Y., Diao, F., Fu, Y., Liu, C., & Xiong, X. (2021). Slip rate of the seismogenic fault of the 2021 maduo earthquake in western China inferred from gps observations. *Science China Earth Sciences*, *64*(8), 1363–1370. https://doi.org/10.1007/s11430-021-9808-0

Zoback, M. D., & Byerlee, J. D. (1975). The effect of microcrack dilatancy on the permeability of westerly granite. *Journal of Geophysical Research*, *80*(5), 752–755. https://doi.org/10.1029/JB080i005p00752